Physical and chemical properties of deposited airborne particulates over the Arabian Red Sea coastal plain

Johann P. Engelbrecht[1,2], Georgiy Stenchikov[1], P. Jish Prakash[1], Traci Lersch[3], Anatolii Anisimov[1] and Illia Shevchenko[1]

[1]King Abdullah University of Science and Technology (KAUST), Physical Science and Engineering Division (PSE), Thuwal, 23955-6900, Saudi Arabia.

[2]Desert Research Institute (DRI), Reno, Nevada 89512-1095, U.S.A.

[3] RJ Lee Group Inc., Monroeville, Pennsylvania 15146, U.S.A.

Correspondence to: Johann P. Engelbrecht (johann@dri.edu)

Abstract

Mineral dust is the most abundant aerosol, having a profound impact on the Global energy budget. This research continues our previous studies performed on surface soils in the Arabian Peninsula and aims at analyzing mineralogical, physical and chemical composition of dust deposits from the atmosphere at the Arabian Red Sea coast. For this purpose, aerosols deposited from the atmosphere are collected during 2015 at six sites on the campus of the King Abdullah University of Science and Technology (KAUST) situated on the Red Sea coastal plain of Saudi Arabia and subjected to the same chemical and mineralogical analysis we conducted on soil samples. Frisbee deposition samplers with foam inserts were used to collect dust and other deposits, for the period December 2014 to December 2015. The average deposition rate measured at KAUST for this period was 14 g m^{-2} per month, with lowest values in winter and increased deposition rates in August to October. The particle size distributions provide assessments of < 10 μm and < 2.5 μm dust deposition rates, and it is suggested that these furthermore represent proxies for PM_{10} (coarse) and $PM_{2.5}$ (fine) particle size fractions, respectively.

XRD analysis of a subset of samples confirms variable amounts of quartz, feldspars, micas, and halite, with lesser amounts of gypsum, calcite, dolomite, hematite, and amphibole. Freeze-dried samples were re-suspended onto the Teflon® filters for elemental analysis by XRF, while splits from each sample were analyzed for water soluble cations and anions by Ion Chromatography. The dust deposits along the Red Sea coast are most probably a mixture of dust emissions from local soils, and soils imported from distal dust sources. It is not possible to identify the exact origin of deposition samples from the mineralogical and chemical results alone. These aerosol data are the first of their kind from the Red Sea region. They will help assess their potential nutrient input into the Red Sea, as well the impact on human health, industry, and solar panel efficiency. These data will also support dust modeling in this important dust belt source area, by better quantifying dust mass balance and optical properties of airborne dust particles.

Keywords

Dust mineralogy, chemistry, particle size distribution
Frisbee deposition samplers
Freeze-dry dust retrieval
Dust deposition rates, AOD and visibility
Proxies for PM_{10} and $PM_{2.5}$ deposition rates

1. Introduction

Dust emission and deposition modeling and measurements are required for the assessment of the dust mass budget. Both emission and deposition are under constrained in atmospheric dust models, leading to large uncertainties (Bergametti and Forêt, 2014; Schulz et al., 2012). To improve simulations, the above authors and others suggested the establishment of dust deposition networks in the vicinity of and away from dust source regions, operating throughout the year. In this paper we are presenting results from a network of dust deposition samplers located on the campus of the King Abdullah University of Science and Technology (KAUST) along the Red Sea coast of Saudi Arabia. This is an important dust source region (Ginoux et al., 2012; Prospero et al., 2002), the effect of which extends thousands of kilometers downwind. To better characterize optical, microphysical, and health effects of dust aerosols we conducted detailed chemical, mineralogical and particle size analysis of deposition samples collected from the air.

1.1 Importance of mineral dust

Mineral dust is the most abundant atmospheric aerosol, primarily from suspended soils in arid and semi-arid regions on Earth (Buseck et al., 2000; Washington and Todd, 2005; Goudie, 2006; Muhs et al., 2014), including deserts of the Arabian Peninsula (Edgell, 2006). Dust aerosols profoundly affect climate (Haywood and Boucher, 2000; Hsu et al., 2004; Kumar et al., 2014), cloud properties (Twomey et al., 1984; Wang et al., 2010; Huang et al., 2006), visibility (Kavouras et al., 2009; Moosmüller et al., 2005), air quality (Hagen and Woodruff, 1973), atmospheric chemistry and mineralogy (Sokolik and Toon, 1999; Kandler et al., 2007), biogeochemical cycles in the ocean and over land (Jickells et al., 2005; Mahowald, 2009), human health (Bennett et al., 2006; Bennion et al., 2007; De Longueville et al., 2010; Menéndez et al., 2017), and agriculture (Fryrear, 1981; Nihlen and Lund, 1995).

A further important implication of dust emission/deposition processes is associated with the harvesting of the solar renewable energy in the desert areas. Dust deposits on solar panels are known to have a severe detrimental effect on the efficiency of photovoltaic systems (Goossens and Van Kerschaever, 1999; Hamou et al., 2014; Mejia et al., 2014; Rao et al., 2014; Sulaiman et al., 2014; Ilse et al., 2016), with its adverse effects depending on mineral composition and atmospheric conditions.

1.2 Importance of dust mineralogy

The importance of dust mineralogy was long been recognized (Engelbrecht et al., 2016), but only recently the explicit transport of different mineralogical species is implemented in climate models (Perlwitz et al., 2015b, a; Scanza et al., 2015)

The mineralogy and chemical composition of dust generated from the Red Sea coastal region remains uncertain. The Red Sea coastal plain is a narrow highly heterogeneous piedmont area, and existing soil databases do not have the spatial resolution to represent it adequately (Nickovic et al., 2012).

The specific objective of the present study is to examine mineralogical, chemical and morphological information of deposition samples collected on the KAUST campus. This will help to better quantify the ecological impacts, health effects, damage to property, and optical effects of dust blown across this area (Engelbrecht et al., 2009b, a; Weese and Abraham, 2009). Knowledge of the mineralogy of the dust deposits will provide information on refractive indices, which can be used to calculate dust optical properties, providing input into radiative transfer models, and to assess the impact of dust events on the Red Sea and adjacent coastal plain.

1.3 Previous dust studies in the region

This research complements our dust studies performed in the Arabian Peninsula (Engelbrecht et al., 2009b; Kalenderski et al., 2013; Prakash et al., 2015; Prakash et al., 2016) and globally (Engelbrecht et al., 2016).

The Arabian Peninsula is one of Earth's major sources of atmospheric dust, contributing as much as 11.8 % (22–500 Mt a^{-1}) of the total (1,877–4000 Mt a^{-1}) global dust emissions (Tanaka and Chiba, 2006). The Red Sea, being enveloped by the Arabian and African deserts is strongly impacted by windborne mineral dust. Along with profound influence on the surface energy budget over land and the Red Sea (Kalenderski et al., 2013; Osipov et al., 2015; Brindley et al., 2015), dust is an important source of nutrients, more so for the oligotrophic northern Red Sea waters (Acosta et al., 2013). From preliminary assessments it is estimated that 5 to 6 major dust storms per year impact the Red Sea region, depositing about 6 Mt of mineral dust into the Red Sea (Prakash et al., 2015). Simulations and satellite observations suggest that the coastal dust

contribution to the total deposition flux into the Red Sea could be substantial, even during fair weather conditions (Jiang et al., 2009; Anisimov et al., 2017). Therefore, the correct representation of the regional dust balance over the Red Sea coastal plain is especially important. Here we specifically focus on the dust deposition in this area, which helps to constrain the dust mass balance, as well as the dust mineralogy and chemical composition. Dust sources impacting on the Arabian Red Sea coastal region were shown to vary by season, coming from local haboobs and low level jets, delivered from the Tokar delta of Sudan in summer (Kalenderski and Stenchikov, 2016), and transported from the west coast of the Arabian Peninsula (Kalenderski et al., 2013).

Minerals previously identified in continental soils from Middle East dust generating regions include quartz, feldspars, calcite, dolomite, micas, chlorite, kaolinite, illite, smectite, palygorskite, mixed-layer clays, vermiculite, iron oxides, gypsum, hornblende and halite (Engelbrecht et al., 2009a; Engelbrecht et al., 2016; Goudie, 2006; Prakash et al., 2016; Pye, 1987; Scheuvens and Kandler, 2014). It could be expected that similar mineral assemblages would occur in variable proportions in the dust deposition samples collected in the region.

2. Meteorology and climate

With the exception of the area around Jazan in the south, which is impacted by the Indian Ocean monsoon, the Red Sea coastal region has a desert climate characterized by extreme heat. Temperatures measured at the KAUST campus reach 43° C during the summer days, with a drop in night-time temperatures on average of more than 10° C. Although the extreme temperatures here are moderated by the proximity of the Red Sea, summer humidity is often 85 % or higher during periods of the northwesterly *Shamal* winds. Rainfall diminishes from an annual average of 133 mm at Jazan in the south to 56 mm at Jeddah, and 24 mm at Tabuk in the north. http://worldweather.wmo.int/en/city.html?cityId=699.

Vegetation is sparse, being restricted to semi-desert shrubs, and acacia trees along the ephemeral rivers (wadis), providing forage for small herds of goats, sheep and dromedary camels.

During infrequent but severe rainstorms, run-off from the escarpment along wadis produce flash floods in lowland areas. With such events, fine silt and clay deposits are formed on the coastal plain, which are transformed into dust sources during dry and windy periods of the year. The resultant dust is transported and deposited along the coastal plain itself and adjacent Red Sea, by

prevailing northwesterly to southwesterly winds, with moderate breezes (wind speed >5.5 m s^{-1}) at the coast (http://www.windfinder.com/weather-maps/report/saudiarabia#6/22.999/34.980).

3. Objectives

This study is meant to complement the recently published papers by our research group that characterize the effect of dust storms (Prakash et al., 2015; Kalenderski et al., 2013), evaluate radiative effect of dust (Osipov et al., 2015), analyze soils from the Red Sea coastal plain (Prakash et al., 2016) and dust emissions in the same region (Anisimov et al., 2017). It aims to provide mineralogical, physical and chemical compositions of deposition samples collected largely during 2015 at six sites on the campus of KAUST, located approximately 80 km north of Jeddah, along the central part of the Red Sea coastal plain of Saudi Arabia, (Fig. 1).

3.1 Regional dust sources

The coastal plains of the Arabian Peninsula along the Red Sea and Persian Gulf are among the most populated areas in this region, hosting several major industrial and residential centers. Airborne dust profoundly affects human activities, marine and land ecosystems, climate, air-quality, and human health. Satellite observations suggest that the narrow Red Sea coastal plain to be an important dust source ~~province~~, augmented by fine sediment accumulations, scattered vegetation, and variable terrain. Airborne dust carries the mineralogical and chemical signature of a parent soil (Prakash et al., 2016). The purpose of a previous study on 13 soil samples from the Arabian Red Sea coastal area (Prakash et al., 2016) was to better characterize their mineralogical, chemical and physical properties, which in turn improve assessment of dust being deposited in the Red Sea and on land, affecting environmental systems and urban centers. It was found that the Red Sea coastal soils contain major components of quartz and feldspar, as well as lesser but variable amounts of amphibole, pyroxene, carbonate, clays, and micas, with traces of gypsum, halite, chlorite, epidote and oxides. The mineral assemblages in the soil samples were ascribed to the variety of igneous and metamorphic provenance rocks of the Arabian Shield forming the escarpment to the east of the coastal plain.

4. Sampling and analysis

Anisimov et al. (2017) estimated that the eastern Red Sea coastal plain emits about 5–6 Mt of dust annually. Due to its close proximity, a significant portion of this dust is likely to be deposited into

the Red Sea, which could be comparable in amount to the estimated annual deposition rate from remote sources during major dust events (Prakash et al., 2015). Therefore, we expect that the total dust deposition into the Red Sea is of the order of 10 Mt a^{-1}, but this figure still needs to be confirmed.

In the past few decades wind tunnel and field tests to compare their efficiencies, had been performed on different designs of deposition samplers and sand traps, including marble dust collectors (MDCO), inverted Frisbees, and glass surfaces (Goossens and Rajot, 2008; Sow et al., 2006; Goossens et al., 2000; Goossens and Offer, 2000). Most of the experiments performed in wind tunnels failed to completely mimic the field conditions, which resulted in an underestimation of the dust deposition, more so for the < 10 μm size fraction (Sow et al., 2006). Based on the field evaluations by Vallack (1995) and suggestions by Vallack and Shillito (1998) the decision was taken to deploy inverted Frisbee samplers with foam inserts.

At each sampling site the particulate deposits were collected into a 227 mm diameter inverted Frisbee dust deposit sampler, each with a polyester foam insert and bird strike preventers (Hall et al., 1993; Vallack and Chadwick, 1992, 1993; Vallack and Shillito, 1998) (Fig. 2). The purpose of the foam insert is to enhance the particulate collection capacity of the dust gauge (Vallack and Shillito, 1998) by better collecting and retaining wet (from fog, dew, rain) and dry, fine and coarse particles being deposited into the inverted Frisbee dish, under stable meteorological conditions, during severe dust events, northwesterly *Shamal* winds, and by daily coastal winds,

For the period December 2014 to March 2015, four Frisbee samplers were located at the New Environmental Oasis (NEO) site, about 50 m apart. The gravimetric information from the four samplers were similar, with small variations amongst them ascribed to the impact from local construction activities. Due to the similarity of these gravimetric results, and to obtain a better representation of dust deposition onto the KAUST campus, two of the samplers (DT1 and DT2) were moved in March, the first (DT1) to a residential area and the other (DT2) to the quay adjacent to the Coastal & Marine Resources Core Lab (CMOR) (Table 1). (Site meta-data provided in the Supplement A).

The deposition samples were collected for intervals of a calendar month, starting in December 2014 and ending December 2015. At the end of each month, the samples are retrieved by flushing

the dust deposit with distilled water from the foam insert and collection dish into the downpipe and plastic bottle. Both the insoluble particles and dissolved salts in the water suspension are retrieved in the laboratory by a freeze-drying (sublimation) procedure.

A total of 52 deposition samples were collected at the six sampling sites on the KAUST campus (Fig. 1b) over a period of 13 months, largely in 2015. Representative subsets of these samples were selected for X-ray diffraction (XRD), (27 samples) and chemical analysis (29 samples).

Freeze-dried sample splits were re-suspended in the laboratory onto Teflon® filters, for elemental analysis by X-ray Fluorescence (XRF) spectrometry by using a miniaturized version of a dust entrainment facility (Engelbrecht et al., 2016), http://www.dri.edu/atmospheric-sciences/atms-laboratories/4185-dust-entrainment-and-characterization-facility). With this modified system the dust sample is drawn into a vertically mounted tubular dilution chamber, and the re-suspended dust collected onto a 47 mm diameter Teflon® filter, for chemical analysis.

The samples re-suspended onto the Teflon® filters were chemically analyzed for elemental content by XRF, including for Si, Ti, Al, Fe, Mn, Ca, K, P, V, Cr, Ni, Cu, Zn, Rb, Sr, Y, Zr, and Pb (US EPA, 1999). Splits of about 2 mg from each freeze-dried sample were analyzed for water soluble cations of sodium (Na^+), potassium (K^+), calcium (Ca^{2+}) and magnesium (Mg^{2+}), and anions of sulfate (SO_4^{2-}), chloride (Cl^-), phosphate (PO_4^{3-}) and nitrate (NO_3^-), by Ion Chromatography (IC) (Chow and Watson, 1999).

A subset of 27 samples from the total of 52 samples, representing all months of the year, was selected for X-ray diffraction (XRD) analysis. XRD is a non-destructive technique particularly suited to identifying and characterizing minerals such as quartz, feldspars, calcite, dolomite, clay minerals and iron oxides, in fine soil and dust. Dust reactivity in seawater as well as optical properties depend on its mineralogy, e.g. carbonates and sulfates are generally more soluble in water than silicates such as feldspars, amphiboles, pyroxenes or quartz. A Bruker D8® X-ray powder diffraction system was used to analyze the mineral content of the dust deposition samples. The diffractometer was operated at 40 kV and 40 mA, with Cu Kα radiation, scanning over a range of 4-50° 2θ. The Bruker Topas® software and relative intensity ratios (RIRs) were applied for semi-quantitative XRD analyses of the dust deposition samples (Rietveld, 1969; Chung, 1974; Esteve et al., 1997; Caquineau et al., 1997; Sturges et al., 1989).

A likely bias in the results from applying the X-ray diffraction (XRD) technique, together with the RIR method is widely recognized, and therefore our methodology is considered to be semi-quantitative at best. Chung (1974) recognized that if the RIRs of all the crystalline phases in a mineral mixture are known, the sum of all the fractions should add to 100 %. However, XRD is effective at measuring crystalline phases such as quartz, calcite, and feldspars, and less so for partly crystalline and amorphous phases, including some layered silicates such as clays as well as many hydrous minerals. This could lead to an overestimation of the abundance of the crystalline mineral species in the dust, compared to partly crystalline and amorphous phases (Formenti et al., 2008; Kandler et al., 2009). Other discrepancies could occur from preferred orientation of layered silicates in the sample mounts. To minimize this effect the dust samples were loaded into side-mount holders.

Electron microscopy provided information on the individual particle size and shape of micron-size particles, important for determining the optical parameters for modeling of dust (Moosmüller et al., 2012). The scanning electron microscope (SEM) based individual particle analysis was performed on a subset of twelve deposition samples collected for each month of 2015. For each sample, the portion of deposition sample was suspended in isopropanol and dispersed by sonication. The suspension was vacuum filtered onto a 0.2 µm pore size polycarbonate substrate. A section of the substrate was mounted onto a metal SEM stub with colloidal graphite adhesive. The sample mounts were sputter-coated with carbon to dissipate the negative charge induced on the sample by the electron beam. The automated analysis was conducted on a Tescan MIRA 3® field emission scanning electron microscope (FE-SEM) by rastering the electron beam over the sample while monitoring the resultant combined backscattered electron (BE) and secondary electron (SE) signals. Based on the grayscale levels, preset threshold values segmented the image into particles of interest and background. The system was configured to automatically measure the size and shape of anywhere from 5,000 to 15,000 particles per sample measuring > 0.2 µm in average diameter. A digital image was acquired of each particle, for measurement, and stored for subsequent review. Size measurements were based on Feret diameters obtained from the projected area of each particle, by tracing their outer edges. This information was used to calculate the shape-dependent particle volumes. The particles were grouped into "bins" by their size. The field emission electron source allows for high magnifications and sharp secondary electron images (SEI), as well as for the detailed study of particle size distributions.

5. Results

5.1 Meteorology

Northwesterly *Shamal* winds prevailed during all twelve months of 2015 (Fig. 3). Four to five severe dust storms lasting three to five days each, contributed to hot humid conditions during the summer months. Weaker northeasterly winds were experienced in October and November of that year. Although the northeasterly winds were more frequent in November, they did not reach the maximum strength of the northwesterlies.

The first four months in the second half of 2015 experienced the highest ambient temperatures (Table 2), with an average temperature of 35^{o} C for August followed by 34^{o} C for September, bracketed by 33^{o} C for both July and October. The highest single temperature was 43^{o} C, recorded in October, with the coolest temperature of 17^{o} C in January of that year. The range of temperatures was the greatest through fall, winter and spring, with large diurnal temperature fluctuations during these seasons. The humidity at KAUST is consistently high (Table 2), with averages varying from 57 % for December and 61% for January, to as high as 82 % for August and 80% for September. Dewpoints were calculated for each set of hourly measurements, applying the August-Roche-Magnus approximation (Alduchov and Eskridge, 1996; August, 1828; Magnus, 1844). The highest dewpoint temperatures were calculated in August (31^{o} C) and September (30^{o} C) while the month with the greatest frequency of humidity measurements (96) in excess of 90 % was also recorded in August (Table 2, Fig. 4). The lowest monthly frequency (4) for humidity exceeding 90 % was December. In 2015, there were only a few light rainfall events at KAUST, and as such not of much importance to our measurements.

5.2 Gravimetric analysis

With a few exceptions, the monthly gravimetric measurements from the four samplers (DT1 – DT4) are comparable (Fig. 5), changing similarly by month and season. The deposition rates were at their lowest for December 2014 (avg. 4 g m^{-2}), increasing steadily for four months to a peak value for March, 2015 (avg. 20 g m^{-2}) before decreasing over the subsequent four months to a low for July (avg. 5 g m^{-2}). The deposition rates increased sharply for August (28 g m^{-2}), September (23 g m^{-2}) and October (28 g m^{-2}), before diminishing in November (14 g m^{-2}) and December (11 g m^{-2}). The NEO terrain is close to several building construction sites, about 400 m to the east and

southeast of the installed deposition samplers, which periodically created substantial amounts of local airborne dust. This, together with the windy conditions are held responsible for elevated dust concentrations measured at the two NEO sites (DT3, DT4). The higher deposition rate at DT3 for August, compared to DT4, is ascribed to the fact that the former sampler is about 100m closer to construction material handling activities during that month. Wind-blown sea spray during stormy conditions was responsible for elevated deposition levels of sea salt at the CMOR (DT2) quay-side site, for the months of September and October 2015.

Bearing in mind that the dust deposition samplers, sampling procedures, as well as conditions and sampling periods were different to those of this study, some comparisons to similar studies in desert regions are listed in Table 3. The deposition rates from this study, both on average (14 g m^{-2} $month^{-1}$) and in range (4-28 g m^{-2} $month^{-1}$), were found to be similar to those previously recorded by Offer and Goossens (2001) in the Negev Desert, Israel (average 17 g m^{-2} $month^{-1}$, range 10-25 g m^{-2} $month^{-1}$), and West Niger (Goossens and Rajot, 2008) (average 13 g m^{-2} $month^{-1}$, range 6-21 g m^{-2} $month^{-1}$). A campaign in the Saudi Arabian capital of Riyadh (Modaihsh, 1997; Modaihsha and Mahjoub, 2013) during the dusty months of January to March showed average monthly deposition rates of 42 g m^{-2} , and a range of 20-140 g m^{-2}. The dust deposition measured in Kuwait on the other hand, varies substantially between sites due to the contribution from disturbed soils in lowlands during periods of north-westerly *Shamal* winds.

5.3 AERONET and visibility measurements

The Aerosol Optical Depth (AOD) is one of the best observed aerosol characteristics. It defines the aerosol radiative effect and reflects the abundance of aerosols in the atmosphere. A CIMEL Robotic Sun Photometer is installed on the rooftop of the CMOR building on the campus of the KAUST and operated by our group since 2012, as a part of the NASA- AERONET, providing aerosol optical depth (AOD) and aerosol retrieved characteristics (https://aeronet.gsfc.nasa.gov/). Figure 6a compares the monthly averaged AOD at 500 nm with the dust deposition rate for 2015. In a general sense the AOD and the deposition rates show comparable trends, both with maxima in spring and larger maxima in fall. However, the AOD reaches a first maximum in April, being one month later than that of the deposition rate. Also, the larger second AOD maximum occurred in August while the maximum deposition rate is broadly distributed over a three-month period, from August to October. The photometer measures light attenuation by all aerosols along a column

in the atmosphere, while deposition rate depends on dust at ground level only, the latter generally containing a relatively coarser dust fraction. The low-level dust particles are partly from local dust sources while the higher altitude dust could be transported from distal sources and chemically transformed, i.e., aged. As was pointed out by Yu et al. (2013) the differences between the deposition and AOD time series can in part be attributed to modifications of the natural dust aerosol by anthropogenic activities, including petrochemical and other large industries along the Red Sea coast, as well as by entrainment of construction and road dust. The linear correlation coefficient between the monthly deposition rates and the monthly averaged AOD of 0.40 suggests a causal interrelationship between these two quantities.

Furthermore, a comparison between the deposition samples and the visibility is made with measurements taken in 2015 at the Jeddah airport meteorological station, approximately 70 km to the south of KAUST. Visibility is expressed as the frequency of dust events with reported weather codes 06-09, or 30–35, grouped as dusty or non-dusty days, for each month (Notaro et al., 2013; Anisimov et al., 2017), expressed as percentages. The bimodal monthly distributions seen with the deposition rates and AERONET monitoring are also mirrored by the visibility measurements collected at Jeddah (Fig. 6b). The linear correlation coefficient between the monthly deposition rates and monthly averaged visibility measurements is 0.48, clearly suggesting a causal relationship between the two variables.

5.4 Particle size distributions (PSD)

Dust deposition rates depend on the meteorological conditions, and dust properties such as particle size distribution, their vertical distribution, and abundance.

Summary plots of results from SEM based individual particle analysis for each month of 2015, expressed by number are presented in the Supplement C to this paper. From these particle size and shape measurements, equivalent shape-dependent volumes for the particles were calculated, the summary plots of which are shown in Appendix A. The volume of each particle is calculated from the measured maximum and minimum diameters, and assuming a prolate spheroid. Also, assuming a similar average density of e.g. 2.65 g cm^{-3} for all minerals in the deposition samples, results in similar volume and mass distributions patterns. This was confirmed by XRD measurements and the abundance of quartz (2.65 g cm^{-1}), feldspar (~ 2.65 g cm^{-1}), micas (~ 2.83 g cm^{-1}), and clays (~

2.7 – 2.8 g cm^{-1}) found in the deposition samples. The volume distributions were applied to assess the mass percentages and deposition rates of each size bin, e.g. the mass percentages and mass deposition rates of particles in bins less < 10 μm in average diameter, and similarly less than < 2.5 μm in average diameter, together with their uncertainties (Table 4). The contribution of particles <10 um to the total measured mass varies between about 4 and 17 % with an average of 8.6 % for the twelve months. Particles less than 2.5 μm range from about 0.6 to 4 %, with an average of 1.2 % for the twelve month period. From these percentages and the total deposition rates, average deposition rates of 1.2±0.7 g m^{-2} $month^{-1}$ for < 10 μm and 0.1±0.1 g m^{-2} $month^{-1}$ for < 2.5 μm are estimated.

The average size distribution of the twelve deposition samples (Fig. 8a) is compared to that of the thirteen surface soils (Fig. 8b) from potential dust source regions along the Red Sea coastal plain (Prakash et al., 2016). The deposition samples with an average diameter of 0.9 μm are much finer than the 3.9 μm average diameter of the < 38 μm sieved soils. In addition the Frisbee sampler is biased towards the sampling of the coarser particles, as previously documented (Bergametti and Forêt, 2014; Goossens, 2005).

5.5 Mineral analysis by XRD

XRD analysis of the 27 samples (Fig. 7) show variable amounts of quartz (6–38 %, avg. 22 %) and feldspars (plagioclase, K-feldspar) (5-34 %, avg. 20 %), clays (10-18 %, avg. 13 %), micas (6-31 %, avg. 13 %), halite (1-53 %, avg. 7 %) with lesser amounts of gypsum (1-8 %, avg. 4 %), calcite (0-8 %, avg. 2 %), dolomite (0-7 %, avg. 3 %), hematite (0-8 %, avg. 3 %), and amphibole (and pyroxene) (0-4%, avg. 1 %).

From the XRD, four broad mineral assemblages are distinguished, the first and major assemblage is comprised of feldspars, clays and micas as well as hematite and gypsum, the second group is of quartz, the third of halite, and the fourth of calcite.

There is an increase in the halite concentrations at sites DT1-DT3, from about 2 % (DT1) in December 2014 to about 53 % (DT2) in July 2015 (Fig. 7). From August onwards there is an abrupt decrease in halite content to less than 5 %, except for samples collected at the DT2 (CMOR,

quay-side) site alongside the ocean. There was a simultaneous increase in the proportion of quartz to a maximum of 38 % in April (DT3), and decreasing to less than 25 % at all sites after July, 2015. The silicate mineral group decreased systematically from about 72 % (DT1) in December 2014 to about 25 % (DT2) in July. Except for two samples from the DT3 site collected in September and October 2015, the dominant minerals after July, 2015 included the silicate assemblage, with concentrations of up to 80 %. The variation in the proportions of the four mineral assemblages, especially the halite, is ascribed to seasonal fluctuations in wind, humidity and precipitation, as well as the proximity of the sea to the sampling sites.

5.6 Chemistry (XRF and IC)

As expected, the chemically analyzed deposition samples contain major amounts of SiO_2 (Appendix A, Fig. 9a, b), varying between 12–53 % (avg. 31 %) in the sample subset, occurring as quartz, and together with Al_2O_3, (avg. 4 %) and CaO, (avg. 2.3 %) in plagioclase, and K_2O (avg. 0.6 %) in potassium feldspars. SiO_2 together with Al_2O_3, Fe_2O_3, TiO_2, MnO, MgO, and some K_2O are also contained in the clays, micas and amphiboles, previously identified in these samples by optical microscopy and XRD. Lesser amounts of CaO are contained in gypsum and calcite, and together with MgO, in dolomite. The iron expressed here as Fe_2O_3 can be contained in hematite (Fe_2O_3), goethite FeO(OH) or in clay minerals such as illite, each with different solubility. It has been suggested that large fractions of iron in soils and dusts are contained as amorphous colloidal coatings on quartz and feldspars (Engelbrecht et al., 2016).

The water-soluble cations (Appendix A, Fig. 10a, b) account for 1-19 % and the anions for 1-30 % of the total mass, respectively. These account for variable amounts of halite (1-32 %), and gypsum (1-9 %), with lesser amounts of other chlorides and carbonates. Of importance as dust borne nutrients likely to be deposited in the Red Sea, are the low concentrations of both water soluble NO_3^- (avg. 0.8 %), and water soluble PO_4^{3-} (avg. 0.2 %) compared to the total P_2O_5 (avg. 0.3 %) in the dust deposits. The phosphorus is contained in the largely insoluble mineral apatite (francolite), found in the sedimentary rocks underlying large parts of the Arabian Peninsula (Notholt et al., 2005).

The sum of chemical species, including elements expressed as oxides, and ion concentrations, vary from 35–78 %, with an average of 56 % of the measured chemical mass. The shortfall from 100 % is attributed in part to components not analyzed for, including H_2O, OH, carbon (CO_3^{2-}, organic carbon, elemental carbon) and artifacts of debris deposited onto the samplers.

The chemical abundances were recalculated as normative minerals (Fig. 11a, b), comparable in composition to those identified by XRD (Fig. 7) and optical microscopy. The relative normative mineral abundances (Fig. 11b) show variable amounts of quartz (avg. 52.4 %) feldspar (avg. 3.9 %), kaolinite (2.6 %), calcite (8.8 %) dolomite (0.2 %), hematite (8.0 %), as well as the evaporate minerals gypsum (12.1 %), halite (12.1 %), sylvite (0.2 %), and bischofite (0.2 %). There is also, as shown by XRD, an increase in halite content from about 7.8 % in January to about 25.9 % in July, followed by a sharp drop to about 4.6 % in August, with greater abundances at the CMOR quayside site in September (51.0 %) and October (31.6 %), ascribed to sea spray from stormy conditions during those two months.

Elemental mass ratios of the Frisbee deposition samples are compared to the <38 μm sieved soil samples from the Arabian Red Sea coastal plain (Prakash et al., 2016), and total suspended particulate (TSP) samples collected at other sites in the Middle East (Engelbrecht et al., 2009b) are compared in Table 5. The average Si/Al ratio of 6.86 of the Frisbee deposition samplers is intermediate to the 13.60 of the Arabian Red Sea coastal soils and the approximately unity of the Middle East samples. The Fe/Al ratios of the sample sets show similar relationships as the Si/Al ratios, being intermediate to the Red Sea coastal soils and four of the five other Middle East countries, excluding UAE to which it is similar. The difference is ascribed to the greater abundance of the minerals such as quartz in the coarser sieved soil samples, and less thereof in the finer TSP fractions. The Ca/Al ratio of 2.17 is similar to those of TSP samples from samples of Qatar (2.07) and UAE (2.16), ascribed to the regional carbonate-bearing soils in all three countries. The average Ti/Al, Mg/Al and K/Al ratios of the Frisbee deposition samples are substantially lower than those of the Red Sea coastal soils, which may be related to mineralogical differences in the dust source regions. Differences can also be ascribed to larger percentages of Al-bearing minerals such as clays in the deposition samples from this study.

6. Summary and conclusions

This study provides new mineralogical, physical and chemical information on deposition samples collected at the KAUST campus during 2015, as well as an assessment of the seasonal variability of the regional dust deposition rates onto Saudi Arabian coastal plain.

Inverted Frisbee samplers with foam inserts are found to be robust, easy to use, and provided comparable results, for the collection of wet and dry deposits. Once a month the samples are retrieved by flushing the deposits into plastic flasks followed by freeze-drying of the slurry and recovery of all suspended particles and dissolved salts. The average deposition rate at KAUST for 2015 was 14 g m^{-2} varying from 4 g m^{-2} in December, to 20 g m^{-2} in March, 5 g m^{-2} in July, 28 g m^{-2} in September and October, and down to 11 g m^{-2} the following December. The changes are ascribed to seasonally variable meteorological conditions, including high humidity prevailing along the Arabian Red Sea coastal plain during the late summer and autumn months. The particle size distributions provide an assessment of <10 μm and < 2.5 μm dust deposition rates, the former varying 0.6-2.8 g m^{-2} and the latter 0.06-0.29 g m^{-2}.per month We suggest these deposition rates as proxies for those of PM_{10} (coarse) and $PM_{2.5}$ (fine), respectively.

Chemical analysis, confirmed by XRD, point to a consistent silicate mineral fractions for the deposition samples, at all sampling sites for the entire sampling period. The Si/Al, Fe/Al, and Ca/Al ratios of the deposition samples fall within the range of the soil samples previously collected along the Arabian Red Sea coastal plain as well as the TSP size fractions collected at several sites in the Middle East. It is proposed that the dust deposits along the Red Sea coast are a mixture of dust emissions from local soils, and soils imported from distal dust sources.

For 2015, there are marked similarities between monthly distribution patterns of the deposition samples and AOD measured at KAUST, as well as visibility measurements from Jeddah airport, 70 km to the south. This shows that both the AOD and visibility measurements mirror fluctuations in dust deposition, although it may not be justified to calculate quantitative interrelationships without further research.

Except for the variable halite fractions and local construction dust, there are small variations in the mineralogical content of the dust samples collected on the KAUST campus. To better model the

dust being deposited in Red Sea, and coastal plain, the sampling campaign should be extended to sites beyond the KAUST campus. Such a sampling site was recently set up on an island off the coast from KAUST. Inclusion of particle size with mineralogical and chemical measurements provide more effective data for the modeling community.

The deposition samplers collect all particle sizes, however bin aerosol models usually consider only PM_{10}. The estimated PM_{10} deposition rates are lower than the total particulate deposition rates we observed. However, the size distribution of deposited particles shown in Figure 8a and Appendix A could be used to assess the contribution of PM_{10} in deposited mass, and reconcile models with observations. Another would be to expand the calculated particle size range in the models to cover TSP. However, this could be computationally expansive.

7. Data availability

The gravimetric, mineralogical and chemical data from this study are available upon request from Georgiy Stenchikov (Georgiy.Stenchikov@kaust.edu.sa).

Author Contributions. Johann Engelbrecht was responsible for the sample analysis and data compilation; Georgiy Stenchikov formulated the problem, designed the research project, and supported experimental activities; Jish Prakash collected, and conducted the freeze-drying of the samples, and performed part of the XRD analysis. Traci Lersch performed the SEM based individual particle analysis, Anatolii Anisimov assembled the meteorological and visibility data; Illia Shevchenko assembled the AERONET optical data; Engelbrecht, Stenchikov, Jish Prakash, Anisimov, and Shevchenko compiled different parts of the manuscript.

Acknowledgements. This research, including the chemical and mineralogical analysis is supported by internal funding from the King Abdullah University of Science and Technology (KAUST). We acknowledge the contributions from the collaborating Core Labs at KAUST, the Desert Research Institute, and RJ Lee Group, Inc. This research is supported by the Supercomputing Laboratory at KAUST.

References

Acosta, F., Ngugi, D. K., and Stingl, U.: Diversity of picoeukaryotes at an oligotrophic site off the Northeastern Red Sea Coast, Aquatic Biosystems, 9, 16, doi: 10.1186/2046-9063-9-16, 2013.

Alduchov, O. A., and Eskridge, R. E.: Improved Magnus Form Approximation of saturation vapor pressure, Journal of Applied Meteorology, 35, 4, 601-609, 1996.

Anisimov, A., Tao, W., Stenchikov, G., Kalenderski, S., Prakash, P. J., Yang, Z., and Shi, M.: Quantifying local-scale dust emission from the Arabian Red Sea coastal plain, Atmospheric Chemistry and Physics, 17, 993-1015, doi:10.5194/acp-17-993-2017, 2017.

August, E. F.: Ueber die Berechnung der Expansivkraft des Wasserdunstes, Annalen der Physik und Chemie, 13, 122-137, 1828.

Bennett, C. M., McKendry, I. G., Kelly, S., Denike, K., and Koch, T.: Impact of the 1998 Gobi dust event on hospital admissions in the Lower Fraser Valley, British Columbia, Science of the Total Environment, 366, 2-3, 918-925, doi: 10.1016/j.scitotenv.2005.12.025, 2006.

Bennion, P., Hubbard, R., O'Hara, S., Wiggs, G., Wegerdt, J., Lewis, S., Small, I., van der Meer, J., and Upshur, R.: The impact of airborne dust on respiratory health in children living in the Aral Sea region, International Journal of Epidemiology, 36, 5, 1103-1110, doi: 10.1093/ije/dym195, 2007.

Bergametti, G., and Forêt, G.: Dust Deposition, in: Mineral Dust. A Key Player in the Earth System, edited by: Knippertz, P., and Stuut, J.-B. W., Springer, Dordrecht, 179-200, 2014.

Brindley, H., Osipov, S., Bantges, R., Smirnov, A., Banks, J., Levy, R., Prakash, P. J., and Stenchikov, G.: An assessment of the quality of aerosol retrievals overthe Red Sea and evaluation of the climatological cloud-free dust direct radiative effect in the region, Journal of Geophysical Research: Atmospheres, 120, 20, 1086210878, doi: 10.1002/2015JD023282, 2015.

Buseck, P. R., Jacob, D. J., Pósfai, M., Li, J., and Anderson, J. R.: Minerals in the air: An environmental perspective, International Geology Review, 42, 7, 577-593, doi: 10.1080/00206810009465101, 2000.

Caquineau, S., Magonthier, M.-C., Gaudichet, A., and Gomes, L.: An improved procedure for the X-ray diffraction analysis of low-mass atmospheric dust samples, European Journal of Mineralogy, 9, 157-166, 1997.

Chow, J. C., and Watson, J. G.: Ion Chromatography in elemental analysis of airborne particles, Elemental Analysis of Airborne Particles, edited by: Landsberger, S., and Creatchman, M., Gordon and Breach Science, Amsterdam, 1999.

Chung, F. H.: Quantitative interpretation of X-ray diffraction patterns of mixtures. I. Matrix-flushing method for quantitative multicomponent analysis, Journal of Applied Crystallography, 7, 519-525, doi:10.1107/S0021889874010375 1974.

De Longueville, F., Hountondji, Y. C., Henry, S., and Ozer, P.: What do we know about effects of desert dust on air quality and human health in West Africa compared to other regions?, Science of the Total Environment, 409, 1, 1-8, doi: 10.1016/j.scitotenv.2010.09.025, 2010.

Edgell, H. S.: Arabian Deserts. Nature, Origin and Evolution, Springer, Dordrecht, Netherlands, 592 pp., 2006.

Engelbrecht, J. P., McDonald, E. V., Gillies, J. A., Jayanty, R. K. M., Casuccio, G., and Gertler, A. W.: Characterizing mineral dusts and other aerosols from the Middle East – Part 2: Grab samples and re-suspensions, Inhalation Toxicology, 21, 327-336, doi: 10.1080/08958370802464299, 2009a.

Engelbrecht, J. P., McDonald, E. V., Gillies, J. A., Jayanty, R. K. M., Casuccio, G., and Gertler, A. W.: Characterizing mineral dusts and other aerosols from the Middle East – Part 1: Ambient sampling, Inhalation Toxicology, 21, 4, 297-326, doi: 10.1080/08958370802464273, 2009b.

Engelbrecht, J. P., Moosmüller, H., Pincock, S., Jayanty, R. K. M., Lersch, T., and Casuccio, G.: Technical Note: Mineralogical, chemical, morphological, and optical interrelationships of mineral dust re-suspensions, Atmospheric Chemistry and Physics, 16, 10809-10830, doi:10.5194/acp-16-10809-2016, 2016.

Esteve, V., Rius, J., Ochando, L. E., and Amigó, J. M.: Quantitative x-ray diffraction phase analysis of coarse airborne particulate collected by cascade impactor sampling, Atmospheric Environment, 31, 23, 3963-3967, doi: 10.1016/S1352-2310(97)00257-4, 1997.

Formenti, P., Rajot, J. L., Desboeufs, K., Caquineau, S., Chevaillier, S., Nava, S., Gaudichet, A., Journet, E., Triquet, S., Alfaro, S., Chiari, M., Haywood, J., Coe, H., and Highwood, E.: Regional variability of the composition of mineral dust from western Africa: Results from the AMMA SOP0/DABEX and DODO field campaigns, Journal of Geophysical Research, 113, doi:10.1029/2008JD009903, 2008.

Fryrear, D. W.: Long-term effect of erosion and cropping on soil productivity, Special Paper - Geological Society of America, 186, 253-260, doi: 10.1130/SPE186-p253, 1981.

Ginoux, P., Prospero, J. M., Gill, T. E., Hsu, N. C., and Zhao, M.: Global-scale attribution of anthropogenic and natural dust sources and their emission rates based on MODIS Deep Blue aerosol products, Reviews of Geophysics, 50, 3, doi:10.1029/2012RG000388, 2012.

Goossens, D., and Van Kerschaever, E.: Aeolian dust deposition on photovoltaic solar cells: The effects of wind velocity and airborne dust concentration on cell performance, Solar Energy, 66, 4, 277-289, 1999.

Goossens, D., Offer, Z., and London, G.: Wind tunnel and field calibration of five aeolian sand traps, Geomorphology, 35, 233-252, http://doi.org/10.1016/S0169-555X(00)00041-6, 2000.

Goossens, D., and Offer, Z. Y.: Wind tunnel and field calibration of six aeolian dust samplers, Atmospheric Environment, 34, 1043-1057, http://doi.org/10.1016/S1352-2310(99)00376-3, 2000.

Goossens, D.: Quantification of the dry aeolian deposition of dust on horizontalsurfaces: an experimental comparison of theory and measurements, Sedimentology, 52, 859-873, doi: 10.1111/j.1365-3091.2005.00719.x, 2005.

Goossens, D., and Rajot, J. L.: Techniques to measure the dry aeolian deposition of dust in arid and semi-arid landscapes: a comparative study in West Niger, Earth Surface Processes and Landforms, 33, 178-195, doi: 10.1002/esp.1533, 2008.

Goudie, A. S., and Middleton, N.J.: Desert Dust in the Global System, Springer, 287 pp., 2006.

Hagen, L. J., and Woodruff, N. P.: Air pollution in the Great Plains, Atmospheric Environment, 7, 323-332, 1973.

Hall, D. J., Upton, S. L., and Marsland, G. W.: Improvements in dust gauge design, in: Measurements of Airborne Pollutants, edited by: Couling, S., Butterworth, Heinemann, 1993.

Hamou, S., Zine, S., and Abdellah, R.: Efficiency of PV module under real working conditions, Energy Procedia, 50, 553-558, 2014.

Haywood, J., and Boucher, O.: Estimates of the direct and indirect radiative forcing due to tropospheric aerosols: A review, Reviews of Geophysics, 38, 4, 513-543, doi: 10.1029/1999RG000078, 2000.

Hsu, N. C., Tsay, S. C., King, M. D., and Herman, J. R.: Aerosol properties over bright-reflecting source regions, IEEE Transactions on Geoscience and Remote Sensing, 42, 3, 557-569, doi: 10.1109/TGRS.2004.824067, 2004.

Huang, J., Minnis, P., Lin, B., Wang, T., Yi, Y., Hu, Y., Sun-Mack, S., and Ayers, K.: Possible influences of Asian dust aerosols on cloud properties and radiative forcing observed from MODIS and CERES, Geophysical Research Letters, 33, L06824, doi: 10.1029/2005GL024724, 2006.

Ilse, K., Werner, M., Naumann, V., Figgis, B. W., Hagendorf, C., and Bagdahn, J.: Microstructural analysis of the cementation process during soiling on glass surfaces in arid and semi-arid climates, Physica Status Solidi RRL, 1-5, doi: 10.1002/pssr.201600152, 2016.

Jiang, H., Farrar, J. T., Beardsley, R. C., Chen, R., and Chen, C.: Zonal surface wind jets across the Red Sea due to mountain gap forcing along both sides of the Red Sea, Geophys. Res. Lett., 36, 19, L19605, 10.1029/2009GL040008, 2009.

Jickells, T. D., An, Z. S., Andersen, K. K., Baker, A. R., Bergametti, G., Brooks, N., Cao, J. J., Boyd, P. W., Duce, R. A., Hunter, K. A., Kawahata, H., Kubilay, N., laRoche, J., Liss, P. S., Mahowald, N., Prospero, J. M., Ridgwell, A. J., Tegen, I., and Torres, R.: Global iron

connections between desert dust, ocean biogeochemistry, and climate, Science, 308, 5718, 67-71, doi: 10.1126/science.1105959, 2005.

Kalenderski, S., Stenchikov, G., and Zhao, C.: Modeling a typical winter-time dust event over the Arabian Peninsula and the Red Sea, Atmospheric Chemistry and Physics, 13, 1999-2014, doi:10.5194/acp-13-1999-2013, 2013.

Kalenderski, S., and Stenchikov, G.: High-resolution regional modeling of summertime transport and impact of African dust over the Red Sea and Arabian Peninsula, Journal of Geophysical Research: Atmospheres, 121, 6435–6458, doi:10.1002/2015JD024480, 2016.

Kandler, K., Benker, N., Bundke, U., Cuevas, E., Ebert, M., Knippertz, P., Rodríguez, S., Schütz, L., and Weinbruch, S.: Chemical composition and complex refractive index of Saharan mineral dust at Izaña, Tenerife (Spain) derived by electron microscopy, Atmospheric Environment, 41, 8058-8074, 2007.

Kandler, K., Schütz, L., Deutscher, C., Ebert, M., Hofmann, H., Jäckel, S., Jaenicke, R., Knippertz, P., Lieke, K., Massling, A., Petzold, A., Schladitz, A., Weinzierl, B., Wiedensohler, A., Zorn, S., and Weinbruch, S.: Size distribution, mass concentration, chemical and mineralogical composition and derived optical parameters of the boundary layer aerosol at Tinfou, Morocco, during SAMUM 2006, Tellus, 61B, 32-50, 2009.

Kavouras, I. G., Etyemezian, V., DuBois, D. W., Xu, J., and Pitchford, M.: Source reconciliation of atmospheric dust causing visibility impairment in class I areas of the western United States, Journal of Geophysical Research-Atmospheres, 114, D02308, 2009.

Kumar, R., Barth, M. C., Pfister, G. G., Naja, M., and Brasseur, G. P.: WRF-Chem simulations of a typical pre-monsoon dust storm in northern India: influences on aerosol optical properties and radiation budget, Atmospheric Chemistry and Physics, 14, 2431-2446, doi: 10.5194/acp-14-2431-2014, 2014.

Magnus, G.: Versuche über die Spannkräfte des Wasserdampfs, Annalen der Physik und Chemie, 61, 2, 225-247, 10.1002/andp.18441370202, 1844.

Mahowald, N., S. Engelstaedter, C. Luo, A. Sealy, P. Artaxo, C. Benitez-Nelson, S. Bonnet, Y. Chen, P.Y. Chuang, D.D. Cohen, F. Dulac, B. Herut, A.M. Johansen, N. Kubilay, R. Losno, W. Maenhaut, A. Paytan, J.M. Prospero, L.M. Shank, and R.L. Siefert: Atmospheric iron deposition: Global distribution, variability and human perturbations, Annual Review of Marine Science, 1, 245-278, doi: 10.1146/annurev.marine.010908.163727, 2009.

Mejia, F., Kleissl, J., and Bosch, J. L.: The effect of dust on solar photovoltaic systems, Energy Procedia, 49, 2370-2376, doi: 10.1016/j.egypro.2014.03.251, 2014.

Menéndez, I., Derbyshire, E., Carrillo, T., Caballero, E., Engelbrecht, J. P., Romero, L. E., Mayer, P. L., de_Castro, F. R., and Mangas, J.: Saharan dust and the impact on adult and elderly allergic patients: the effect of threshold values in the northern sector of Gran Canaria, Spain, International Journal of Environmental Health Research, 27, 2, 144-160, doi: 10.1080/09603123.2017.1292496, 2017.

Modaihsh, A. S.: Characteristics and composition of the falling dust sediments on Riyadh City, Saudi Arabia, Journal of Arid Environments, 36, 2, 211-223, http://dx.doi.org/10.1006/jare.1996.0225, 1997.

Modaihsha, A. S., and Mahjoub, M. O.: Falling dust characteristics in Riyadh City, Saudi Arabia during winter months, Asia-Pacific Chemical, Biological & Engineering Society Procedia, 5, 50-58, doi: 10.1016/j.apcbee.2013.05.010, 2013.

Moosmüller, H., Varma, R., Arnott, W. P., Kuhns, H. D., Etyemezian, V., and Gillies, J. A.: Scattering cross-section emission factors for visibility and radiative transfer applications: Military vehicles traveling on unpaved roads, Journal of the Air and Waste Management Association 55, 1743-1750, 2005.

Moosmüller, H., Engelbrecht, J. P., Skiba, M., Frey, G., Chakrabarty, R. K., and Arnott, W. P.: Single scattering albedo of fine mineral dust aerosols controlled by iron concentration, J. Geophys. Res., 117, D11210, doi:10.1029/2011JD016909, 10.1029/2011JD016909, 2012.

Muhs, D. R., Prospero, J. M., Baddock, M. C., and Gill, T. E.: Identifying sources of aeolian mineral dust: Present and past, in: Mineral Dust, A Key Player in the Earth System, edited by: Knippertz, P., and Stuut, J.-B. W., Springer Science+Business Media Dordrecht, 51-74, 2014.

Nickovic, S., Vukovic, A., Vujadinovic, M., Djurdjevic, V., and Pejanovic, G.: Technical Note: High-resolution mineralogical database of dust-productive soils for atmospheric dust modeling, Atmospheric Chemistry and Physics, 12, 845–855, doi:10.5194/acp-12-845-2012, 2012.

Nihlen, T., and Lund, S. O.: Influence of aeolian dust on soil Formation in the Aegean area, Zeitschrift fur Geomorphologie, 393, 341-361, 1995.

Notaro, M., Alkolibi, F., Fadda, E., and Bakhrjy, F.: Trajectory analysis of Saudi Arabian dust storms, Journal of Geophysical Research: Atmospheres, 118, 6028–6043, doi:10.1002/jgrd.50346, 2013.

Notholt, A. J. G., Sheldon, R. P., and Davidson, D. F.: Phosphate deposits of the world, Volume 2, Phosphate rock resources, Cambridge University Press, New York, 600 pp., 2005.

Offer, Z. Y., and Goossens, D.: Ten years of aeolian dust dynamics in a desert region (Negev Desert, Israel): analysis of airborne dust concentration, dust accumulation and the high-magnitude dust events, Journal of Arid Environments 47, 2, 211-249, http://dx.doi.org/10.1006/jare.2000.0706, 2001.

Osipov, S., Stenchikov, G., Brindley, H., and Banks, J.: Diurnal cycle of the dust instantaneous direct radiative forcing over the Arabian Peninsula, Atmospheric Chemistry and Physics, 15, 9537–9553, doi:10.5194/acp-15-9537-2015, 2015.

Perlwitz, J. P., Pérez García-Pando, C., and Miller, R. L.: Predicting the mineral composition of dust aerosols – Part 2: Model evaluation and identification of key processes with observations, Atmospheric Chemistry and Physics, 15, 20, 11629-11652, doi: 10.5194/acp-15-11629-2015, 2015a.

Perlwitz, J. P., Pérez García-Pando, C., and Miller, R. L.: Predicting the mineral composition of dust aerosols – Part 1: Representing key processes, Atmospheric Chemistry and Physics, 15, 20, 11593–11627, doi: 10.5194/acp-15-11593-2015, 2015b.

Prakash, P. J., Stenchikov, G., Kalenderski, S., Osipov, S., and Bangalath, H.: The impact of dust storms on the Arabian Peninsula and the Red Sea, Atmospheric Chemistry and Physics, 15, 199-222, doi: 10.5194/acp-15-199-2015, 2015.

Prakash, P. J., Stenchikov, G., Tao, W., Yapici, T., Warsama, B., and Engelbrecht, J. P.: Arabian Red Sea coastal soils as potential mineral dust sources, Atmospheric Chemistry and Physics, 16, 18, 11991-12004, doi:10.5194/acp-16-11991-2016, 2016.

Prospero, J. M., Ginoux, P., Torres, O., Nicholson, S. E., and Gill, T. E.: Environmental characterization of global sources of atmospheric soil dust identified with the Nimbus 7 Total Ozone Mapping Spectrometer (TOMS) absorbing aerosol product, Reviews of Geophysics, 40, 1, doi:10.1029/2000RG000095, 2002.

Pye, K.: Aeolian dust and dust deposits, Academic Press, London, 1987.

Rao, A., Pillai, R., Mani, M., and Ramamurthy, P.: Influence of dust deposition on photovoltaic panel performance, Energy Procedia, 54, 690-700, doi: 10.1016/j.egypro.2014.07.310, 2014.

Rietveld, H. M.: A profile refinement method for nuclear and magnetic structures, Journal of Applied Crystallography, 2, 65-71, dx.doi.org/10.1107/S0021889869006558, 1969.

Scanza, R. A., Mahowald, N., Ghan, S., Zender, C. S., Kok, J. F., Liu, X., Zhang, Y., and Albani, S.: Modeling dust as component minerals in the Community Atmosphere Model: development of framework and impact on radiative forcing, Atmospheric Chemistry and Physics, 15, 537-561, doi:10.5194/acp-15-537-2015, 2015.

Scheuvens, D., and Kandler, K.: On composition, morphology, and size distribution of airborne mineral dust, in: Mineral Dust, a Key Player in the Earth System, edited by: Knippertz, P., and Stuut, J.-B. W., Springer Science+Business Media Dordrecht, 15-49, 2014.

Schulz, M., Prospero, J. M., Baker, A. R., Dentener, F., Ickes, L., Liss, P. S., Mahowald, N. M., Nickovic, S., García-Pando, C. P., Rodríguez, S., Sarin, M., Tegen, I., and Duce, R. A.: Atmospheric transport and deposition of mineral dust to the ocean: implications for research needs, Environmental Science & Technology, 46, 19, 10390-10404, doi: 10.1021/es300073u, 2012.

Sokolik, I. N., and Toon, O. B.: Incorporation of mineralogical composition into models of the radiative properties of mineral aerosol from UV to IR wavelengths, Journal of Geophysical Research - Atmospheres, 104, D8, 9423-9444, doi: 10.1029/1998JD200048, 1999.

Sow, M., Goossens, D., and Rajot, J. L.: Calibration of the MDCO dust collector and of four versions of the inverted frisbee dust deposition sampler, Geomorphology, 82, 3, 360-375, doi: 10.1016/j.geomorph.2006.05.013, 2006.

Sturges, W. T., Harrison, R. M., and Barrie, L. A.: Semi-quantitative X-ray diffraction analysis of size fractionated atmospheric particles, Atmos. Env., 23, 5, 1083-1098, 1989.

Sulaiman, S. A., Singh, A. K., Mokhtar, M. M. M., and Bou-Rabee, M. A.: Influence of dirt accumulation on performance of PV panels, Energy Procedia, 50, 50-56, doi: 10.1016/j.egypro.2014.06.006, 2014.

Tanaka, T. Y., and Chiba, M.: A numerical study of the contributions of dust source regions to the global dust budget, Global and Planetary Change, 52, 1-4, 88-104, doi:10.1016/j.gloplacha.2006.02.002, 2006.

Twomey, S. A., Piepgrass, M., and Wolfe, T. L.: An assessment of the impact of pollution on global cloud albedo, Tellus B, 36B, 5, 356-366, doi: 10.1111/j.1600-0889.1984.tb00254.x, 1984.

US EPA: Compendium of Methods for the Determination of Inorganic Compounds in Ambient Air, Compendium Method IO-3.3, Determination of metals in ambient particulate matter using X-ray fluorescence (XRF) spectroscopy, EPA/625/R-96/010, 3.3-1 - 3.3-32, 1999.

Vallack, H. W., and Chadwick, M. J.: A field comparison of dust deposit gauge performance at two sites in Yorkshire, Atmospheric Environment Part A, 26, 8, 1445-1451, https://doi.org/10.1016/0960-1686(92)90129-9, 1992.

Vallack, H. W., and Chadwick, M. J.: Monitoring airborne dust in a high density coal-fired power station region in North Yorkshire, Environmental Pollution, 80, 2, 177-183, https://doi.org/10.1016/0269-7491(93)90145-E, 1993.

Vallack, H. W.: A field evaluation of Frisbee-type dust deposit gauges, Atmospheric Environment, 29, 12, 1465-1469, https://doi.org/10.1016/1352-2310(95)00079-E, 1995.

Vallack, H. W., and Shillito, D. E.: Suggested guidelines for deposited ambient dust, Atmospheric Environment, 32, 16, 2737-2744, http://doi.org/10.1016/S1352-2310(98)00037-5, 1998.

Wang, W., Huang, J., Minnis, P., Hu, Y., Li, J., Huang, Z., Ayers, J. K., and Wang, T.: Dusty cloud properties and radiative forcing over dust source and downwind regions derived from A-Train data during the Pacific Dust Experiment, Journal of Geophysical Research, 115, D00H35, doi: 10.1029/2010JD014109, 2010.

Washington, R., and Todd, M. C.: Atmospheric controls on mineral dust emission from the Bodélé depression, Chad: The role of the low level jet, Geophysical Research Letters, 32, L17701,, doi:10.1029/2005GL023597, 2005.

Weese, C. B., and Abraham, J. H.: Potential health implications associated with particulate matter exposure in deployed settings in southwest Asia, Inhalation Toxicology, 21, 291-296, doi: 10.1080/08958370802672891, 2009.

Yu, Y., Notaro, M., Liu, Z., Kalashnikova, O., Alkolibi, F., Fadda, E., and Bakhrjy, F.: Assessing temporal and spatial variations in atmospheric dustover Saudi Arabia through satellite, radiometric, and station data, Journal of Geophysical Research, Atmospheres, 118, 13,253–213,264, doi:10.1002/2013JD020677, 2013.

FIGURES

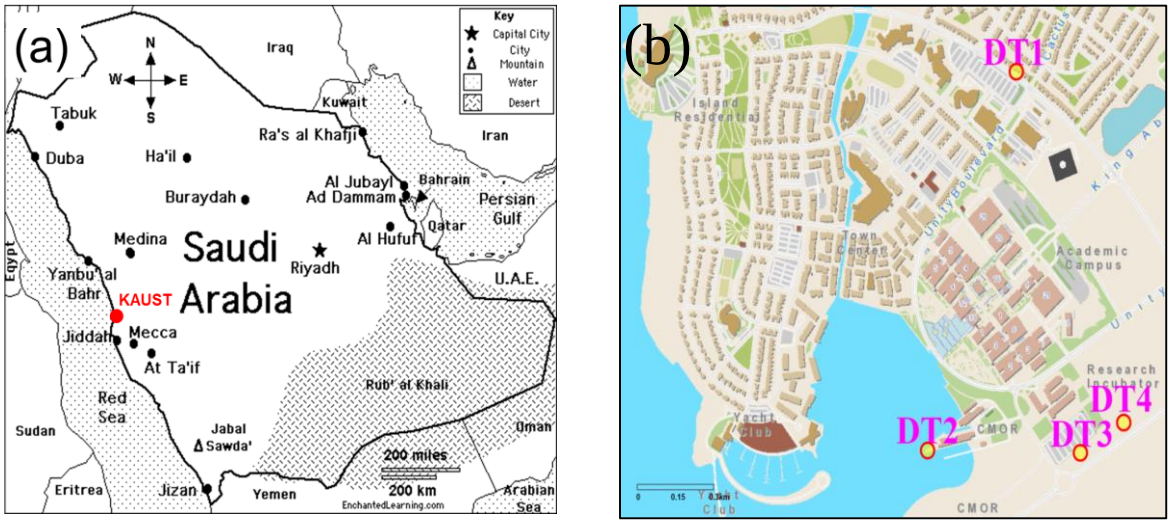

Figure 1. Position of (a) the King Abdullah University of Science and Technology (KAUST) campus on the Arabian Peninsula (red marker), north of the coastal city of Jeddah and (b) the Frisbee deposition sites (DT1-DT4) on the KAUST campus.

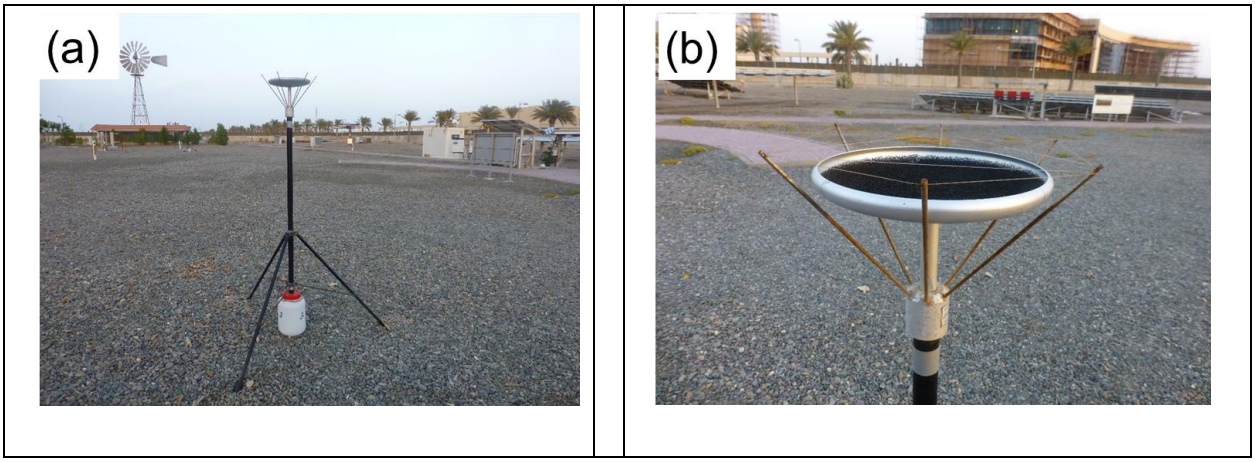

Figure 2. Inverted Frisbee type deposition sampler (a) on tripod and white plastic drainage bottle, (b) showing the foam insert in the collection dish to help retain the deposited dust particles, as well as the spikes with nylon thread to prevent birds from readily perching on the dish.

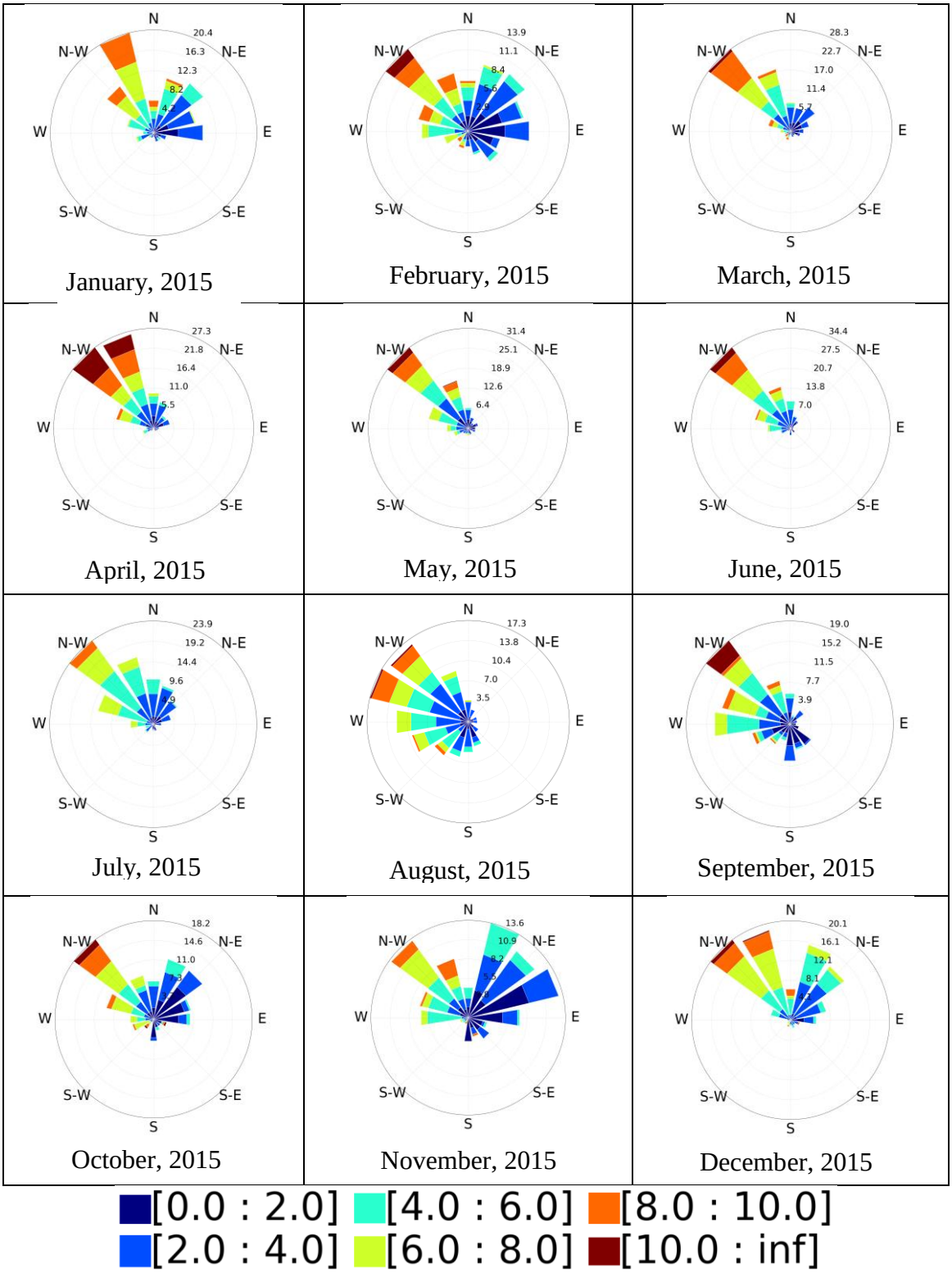

Figure 3. Wind (m s^{-1}) roses for each month of 2015.

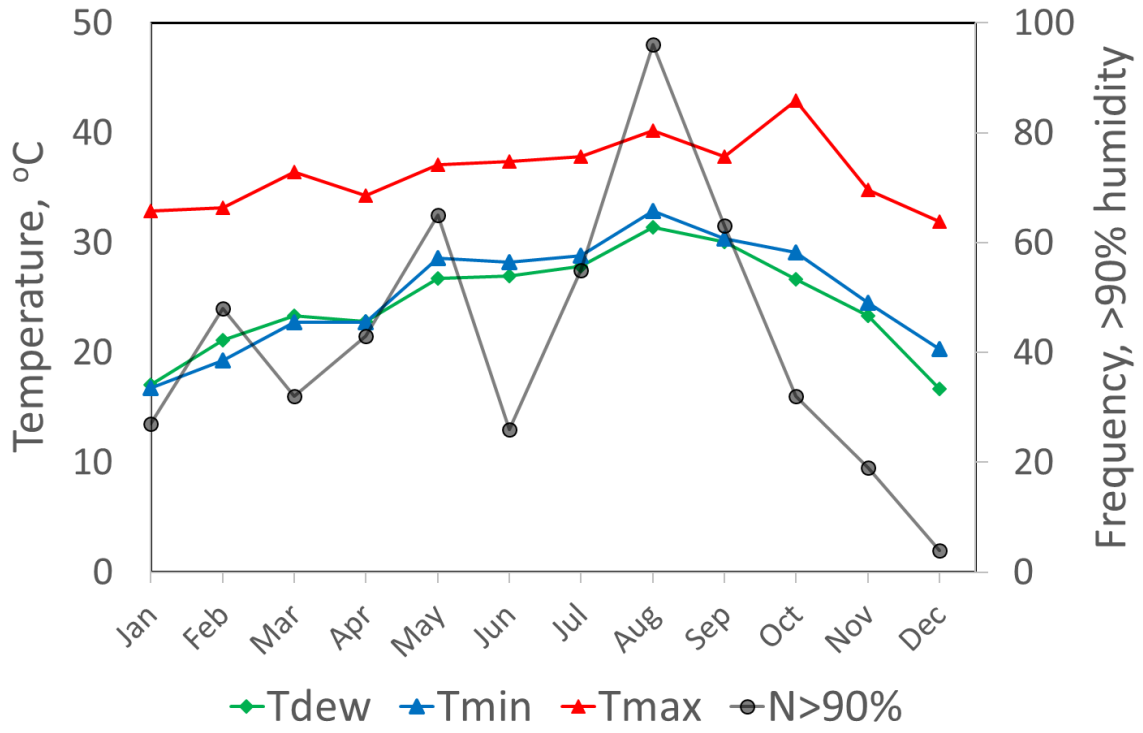

Figure 4. Monthly averaged minimum (——) and maximum (——) ambient temperatures as well as dewpoint (——) variations for KAUST during 2015. Also shown for each month is the frequency of hourly humidity measurements exceeding 90% (——).

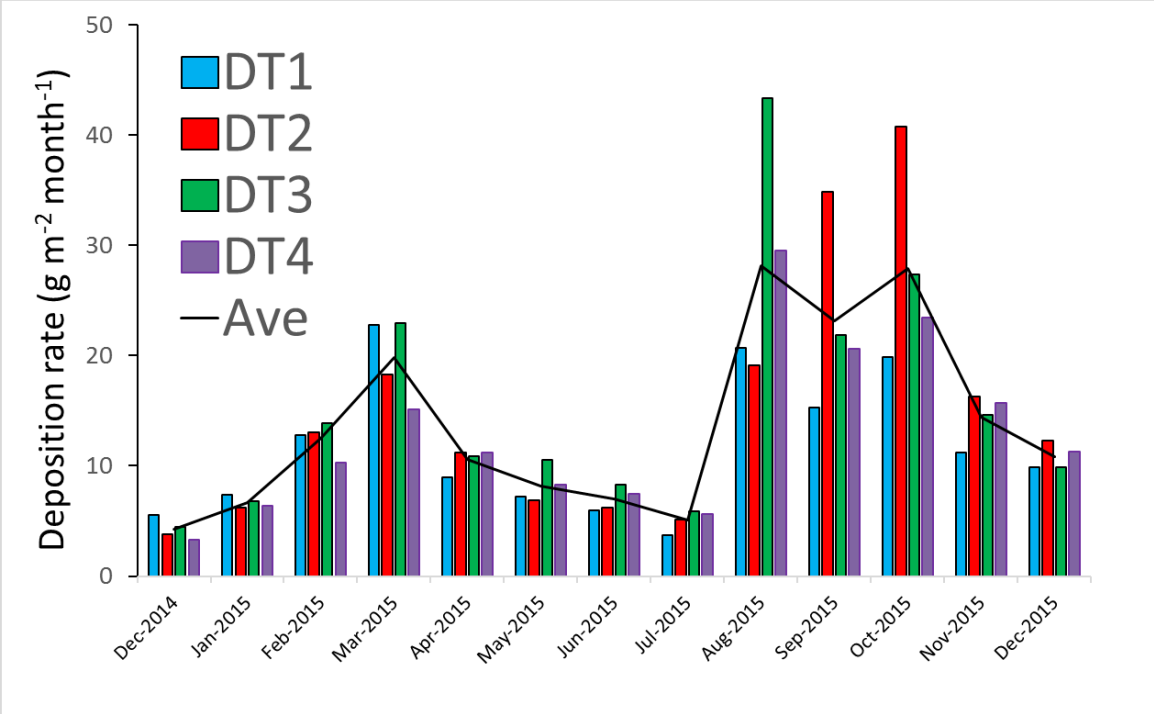

Figure 5. Monthly deposition rates (g m^{-2}) from Frisbee samplers (DT1-DT4) at the KAUST campus. Also shown are the monthly averages for the four samplers.

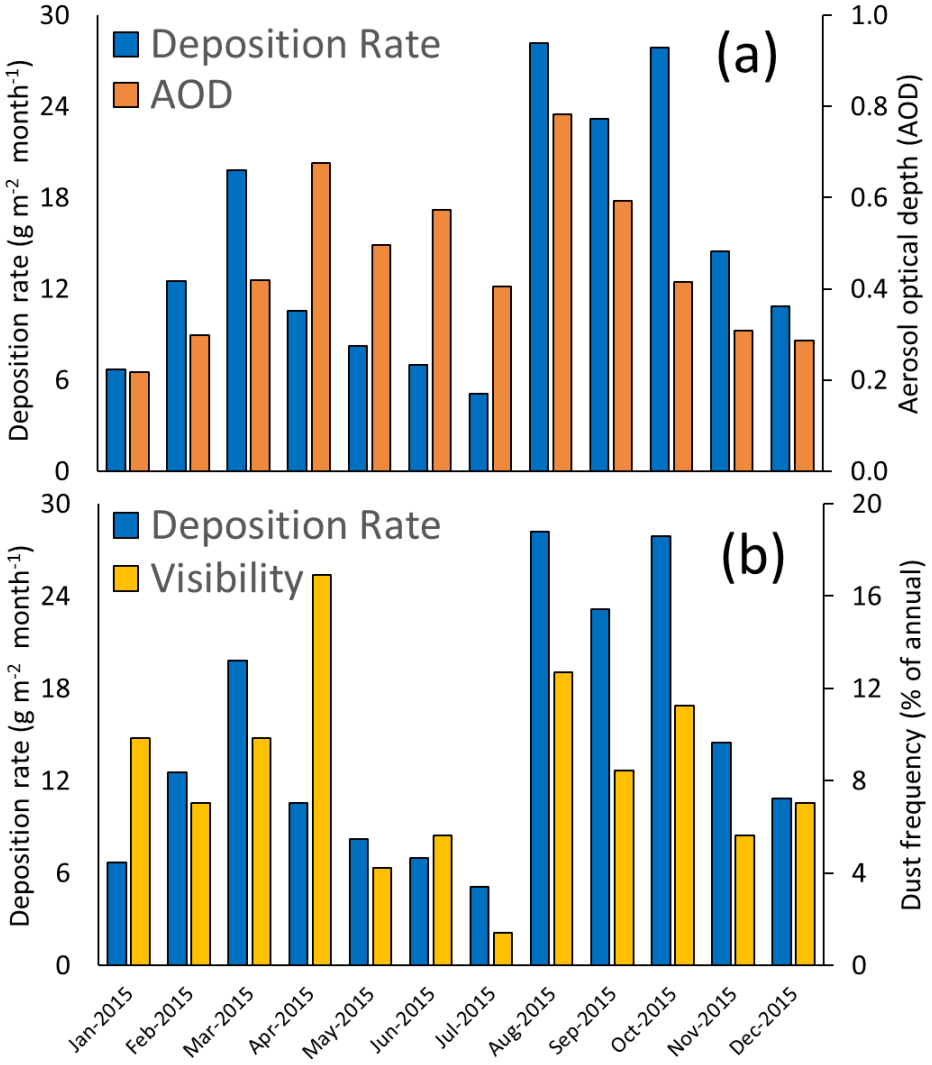

5 Figure 6. Average monthly deposition rates for all four samplers (DT1-DT4) on the KAUST campus, together with (a) monthly averaged AOD measurements from the KAUST AERONET site, and (b) monthly averaged visibility measurements collected from the Jeddah airport, for 2015.

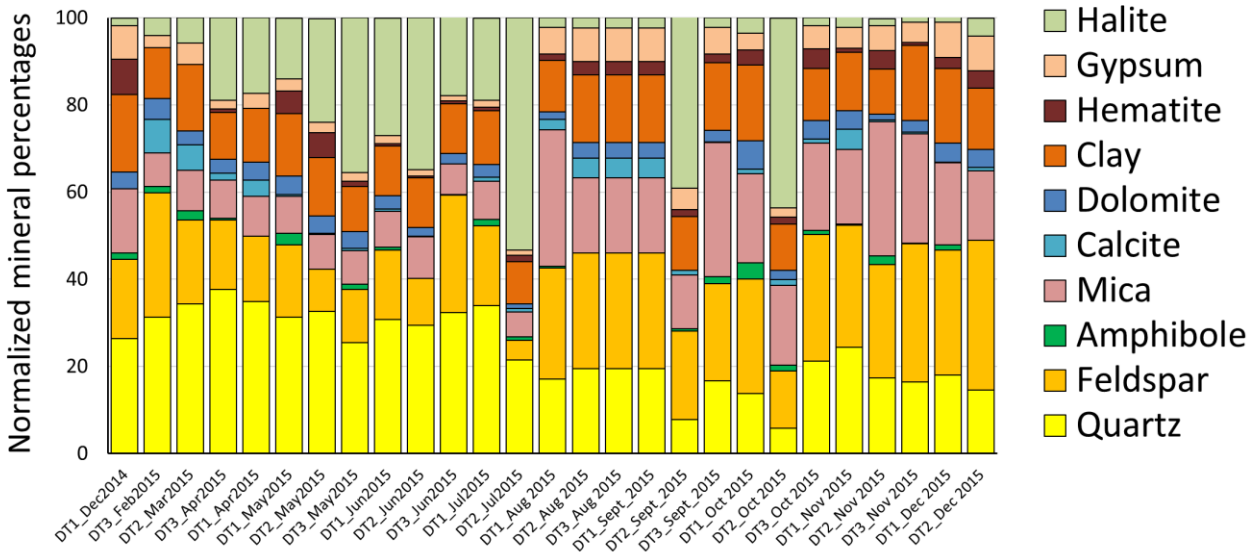

5 Figure 7. Semi-quantitative XRD mineral analyses of monthly Frisbee samples collected at the three sites DT1–DT3, for the period December, 2014 to December2015.

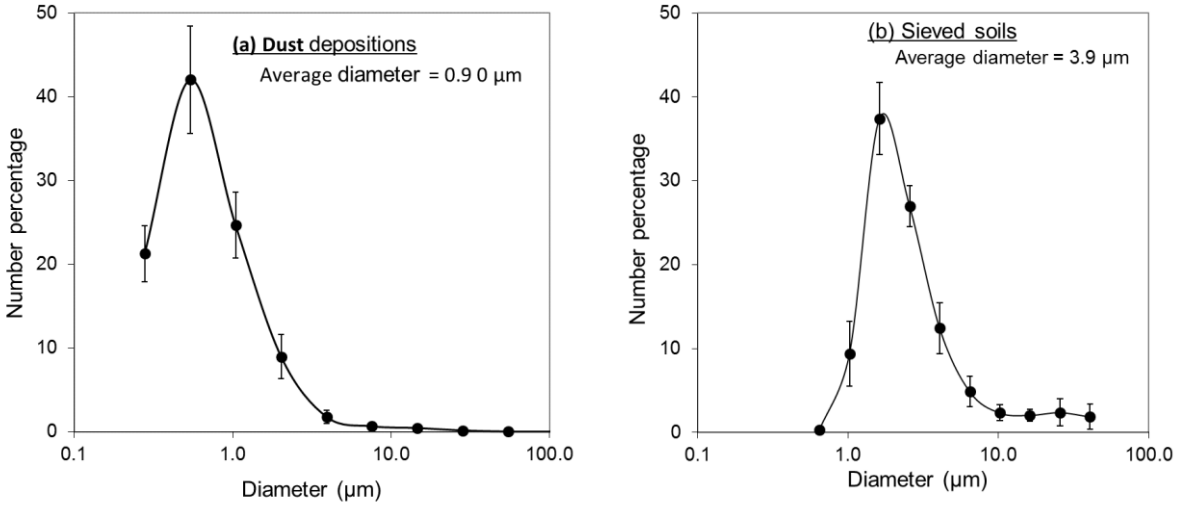

Figure 8. Average particle size distributions and standard deviations of (a) twelve deposition samples collected by Frisbee samplers on KAUST campus, and of (b) thirteen < 38 µm sieved soil samples from a previous study (Prakash et al., 2016), both measured by SEM.

5

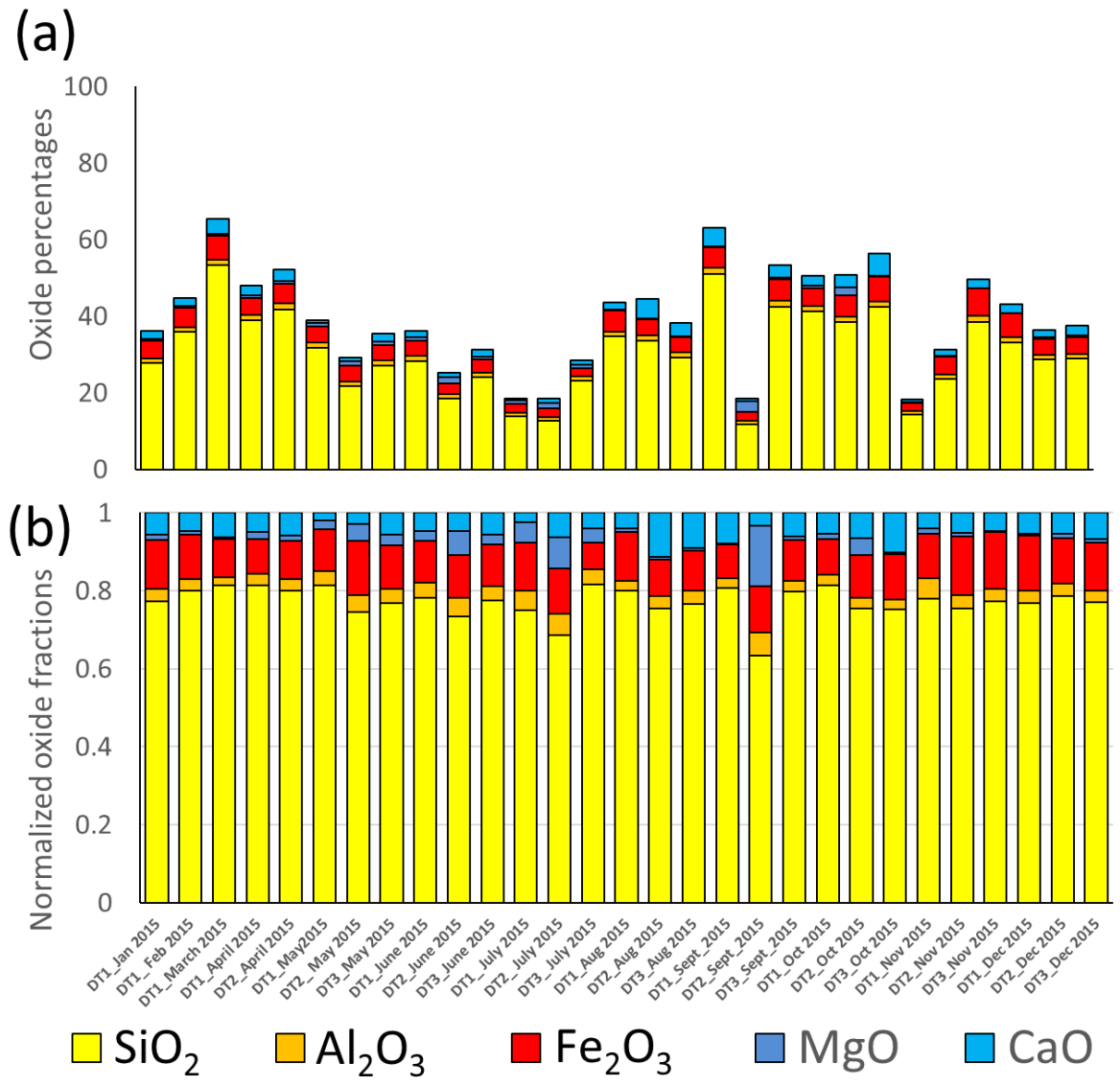

Figure 9 (a). Deposition sample elemental compositions, expressed as oxides and (b) fractions normalized to unity.

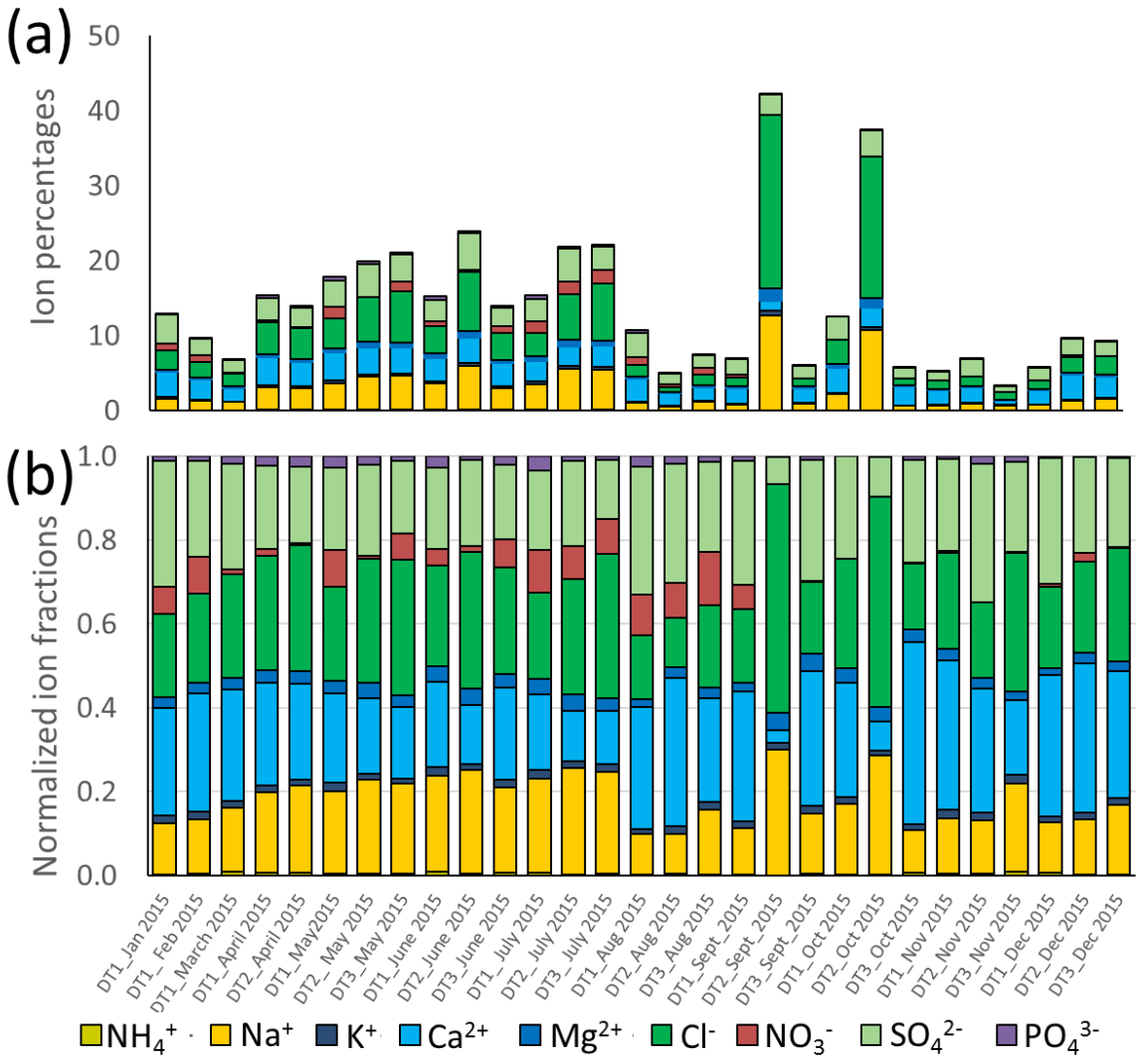

Figure 10 (a). Ion concentrations and (b) fractions totaled to unity.

5

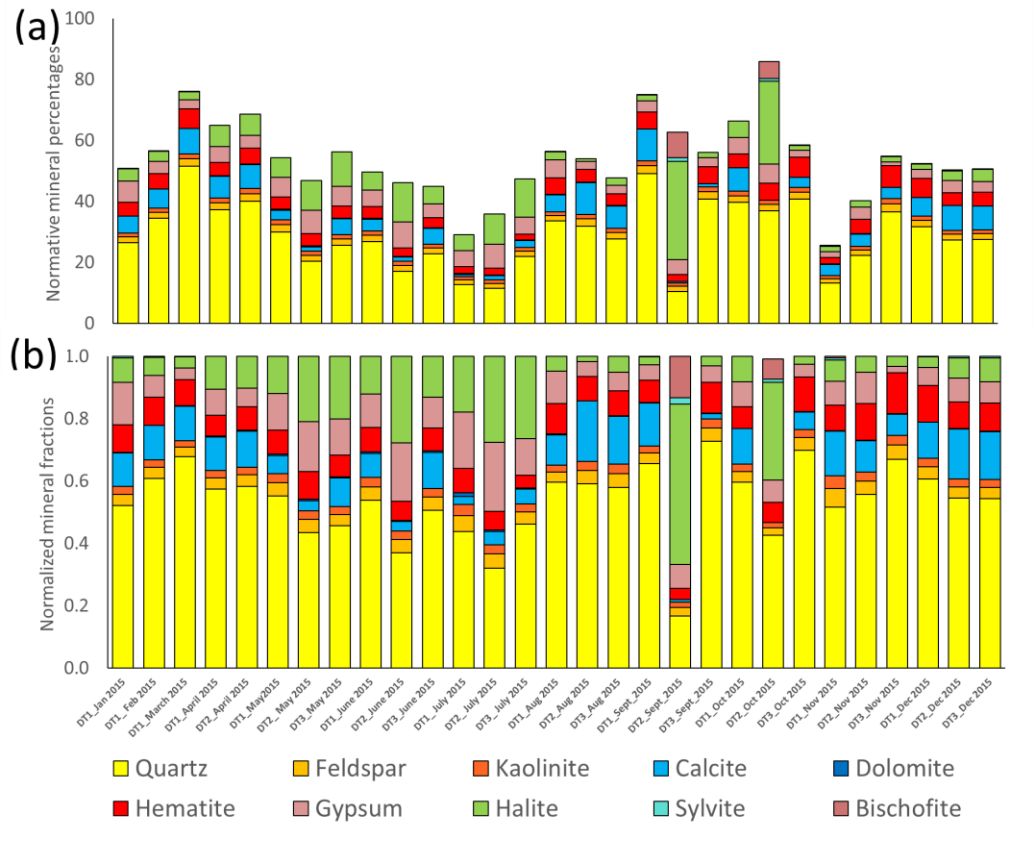

Figure 11 (a). Chemical abundances combined as normative minerals, (b) normalized to 100 %.

5

TABLES

Table 1. Locality of deposition samplers at six sites on the campus of KAUST.

	Site	Latitude	Longitude	Elev. m.a.s.l.	Start	End
DT1	NEO 1	22°18'16.12"N	39°06'28.46"E	1	Dec14	Mar15
	Res G3705	22°18'59.06"N	39°06'21.32"E	12	Apr15	Dec15
DT2	NEO 2	22°18'16.84"N	39° 6'29.33"E	1	Dec14	Mar15
	CMOR	22°18'16.60"N	39° 6'7.91"E	1	Apr15	Dec15
DT3	NEO 3	22°18'17.31"N	39° 6'30.51"E	1	Dec14	Dec15
DT4	NEO 4	22°18'18.10"N	39° 6'31.52"E	1	Dec14	Dec15

Table 2. Monthly averaged temperatures, humidity measurements, and calculated dewpoints at KAUST during 2015.

Month	Temperature				Humidity				Dewpoint
	Avg. °C	Min. °C	Max. °C	Range °C	Avg. %	Min. %	Max. %	N>90% Count	Avg. °C
Jan	25	17	33	16	61	10	99	27	17
Feb	27	19	33	14	74	15	99	48	21
Mar	28	23	36	14	76	29	99	32	23
Apr	28	23	34	12	74	23	99	43	23
May	32	29	37	9	77	21	99	65	27
Jun	32	28	37	9	76	22	99	26	27
Jul	33	29	38	9	75	26	99	55	28
Aug	35	33	40	7	82	36	99	96	31
Sep	34	30	38	8	80	26	99	63	30
Oct	33	29	43	14	72	9	96	32	27
Nov	30	25	35	10	69	25	99	19	23
Dec	27	20	32	12	57	15	94	4	17

Table 3. Dust deposition measurements from the Middle East and other Global dust regions.

	Study	Locality	Sampler type	Sampling period	Average deposition rate (g m^{-2} $month^{-1}$)	Range deposition rate (g m^{-2} $month^{-1}$)
(a)	This study (2017)	Saudi Arabia, KAUST	Frisbee with foam insert	Dec 2014 - Dec 2015	14	4 - 28
(b)	Modaihsh and Mahjoub (2013)	Saudi Arabia, Riyadh	Dish with marbles	Jan - Mar ?	42	20 - 140
(c)	Khalaf and Al-Hashash (1983)	Kuwait, N-W Gulf	Polyethelene cylinders with water	Apr 1979 - Mar 1980	191	10 - 1003
(d)	Al-Awadhi (2005)	Kuwait, N-E Bay	PVC bucket with marbles	May 2002 - Apr 2003	28	3 - 58
(e)	Al-Awadhi and AlShuaibi (2013)	Kuwait, City	PVC bucket with marbles	Mar 2011 - Feb 2012	53	2 - 320
(f)	Offer and Goossens (2001)	Israel, Negev	Marble collectors	1988 - 1997	17	10 - 25
(g)	Goossens and Rajot (2008)	Niger, Banizoumbou	Frisbee with marbles, original data	8 periods in 2005	13	6 - 21
(h)	Smith and Twiss (1965)	USA, Kansas	Cylindrical rain gauge with screens	June 1963 - June 1964	6	3 - 14

Table 4. Monthly measured deposition rates, and assessments of < 10 μm and < 2.5 μm deposition rates from SEM based particle size measurements.

Sample #	Month (2015)	Deposition Rate				
		Total	< 10 μm		< 2.5 μm	
		g m^{-2} $month^{-1}$	% of Total	g m^{-2} $month^{-1}$	% of Total	g m^{-2} $month^{-1}$
DT3.1_012015	January	7.34	16.5 ± 4.3	1.2 ± 0.3	4.0 ± 1.6	0.29 ± 0.12
DT3.1_022015	February	12.83	7.0 ± 3.3	0.9 ± 0.4	0.9 ± 0.4	0.12 ± 0.05
DT3.4_032015	March	15.11	12.0 ± 5.8	1.8 ± 0.9	1.6 ± 0.6	0.24 ± 0.09
DT3.4_042015	April	11.22	8.7 ± 2.8	1.0 ± 0.3	0.8 ± 0.3	0.09 ± 0.03
DT3.3_052015	May	10.51	7.3 ± 2.1	0.8 ± 0.2	0.8 ± 0.3	0.08 ± 0.03
DT3.3_062015	June	8.28	9.0 ± 2.8	0.7 ± 0.2	0.9 ± 0.3	0.07 ± 0.02
DT3.3_072015	July	5.86	9.7 ± 6.3	0.6 ± 0.4	1.1 ± 0.7	0.06 ± 0.04
DT3.3_082015	August	43.39	6.4 ± 3.3	2.8 ± 1.4	0.6 ± 0.4	0.26 ± 0.17
DT3.3_092015	September	21.90	4.3 ± 7.1	0.9 ± 1.6	0.6 ± 1.0	0.13 ± 0.22
DT3.3_102015	October	27.39	9.2 ± 7.3	2.5 ± 2.0	0.8 ± 0.6	0.22 ± 0.16
DT3.3_112015	November	14.59	6.1 ± 1.4	0.9 ± 0.2	0.7 ± 0.2	0.10 ± 0.03
DT3.3_122015	December	9.91	7.3 ± 2.5	0.7 ± 0.2	1.1 ± 0.2	0.11 ± 0.02

Table 5. Elemental mass ratios for the deposition samples from this study, compared to those of soils from the Red Sea coastal plain (Prakash et al., 2016) and TSP samples from other countries of the Middle East (Engelbrecht et al., 2009b). The TSP filter samples were collected by low-volume aerosol samplers without size selective inlets, for 24-hr sampling periods.

		Si/Al	Ti/Al	Fe/Al	Mg/Al	Ca/Al	K/Al
Frisbee	Deposition	6.86	0.14	1.47	0.11	2.17	0.34
Saudi Soils	Sieved <38µm	13.60	0.44	2.52	0.65	0.36	0.43
Djibouti	TSP	0.92	2.19	1.12	0.88	0.74	1.14
Afghanistan	TSP	1.05	1.25	1.00	0.94	0.69	1.96
Qatar	TSP	1.02	0.24	0.98	1.40	2.07	0.93
UAE	TSP	1.29	0.28	1.52	2.85	2.16	1.02
Iraq	TSP	1.03	0.72	0.99	1.11	1.31	1.04
Kuwait	TSP	1.07	0.65	0.99	1.25	1.23	0.94

Appendix A

SEM based particle volume distribution curves for 12 months of 2015

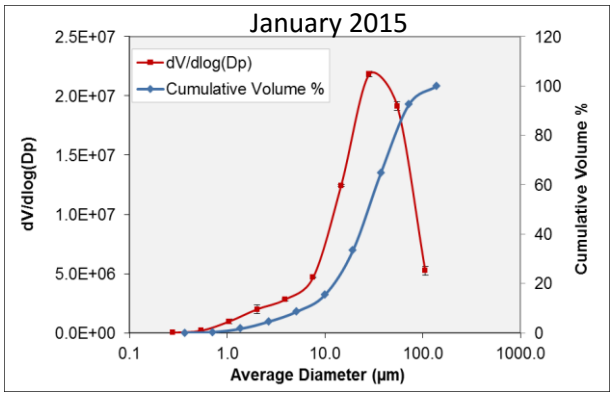

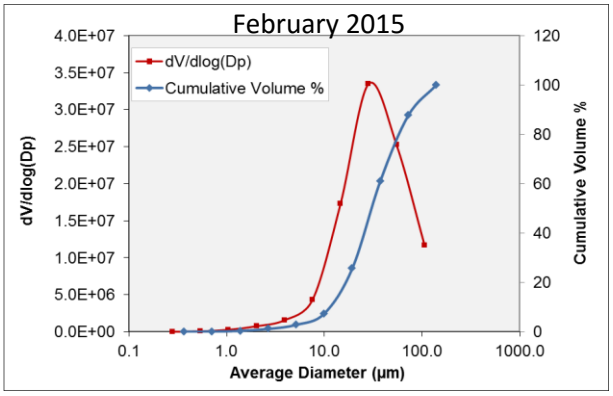

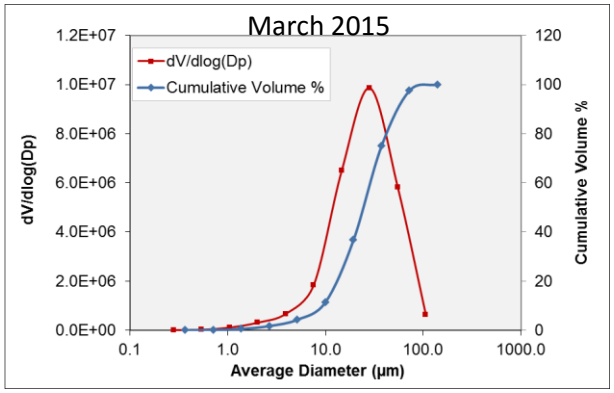

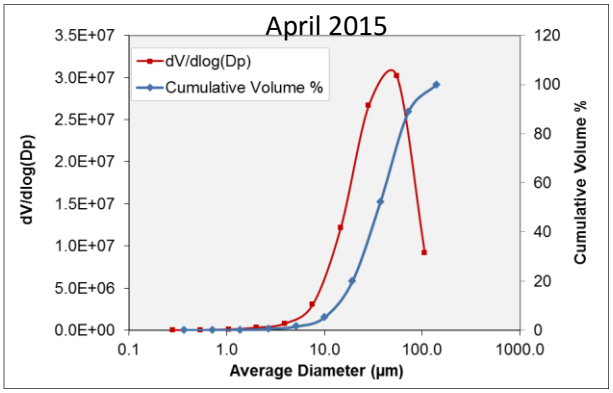

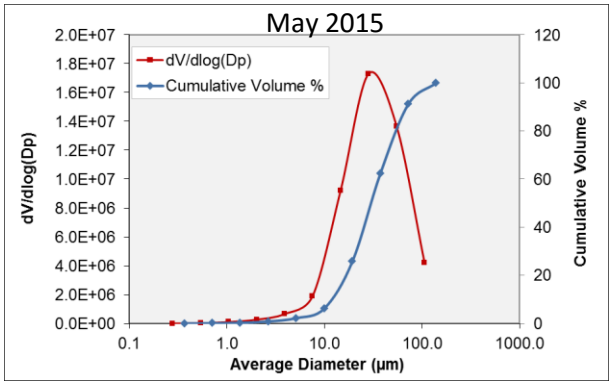

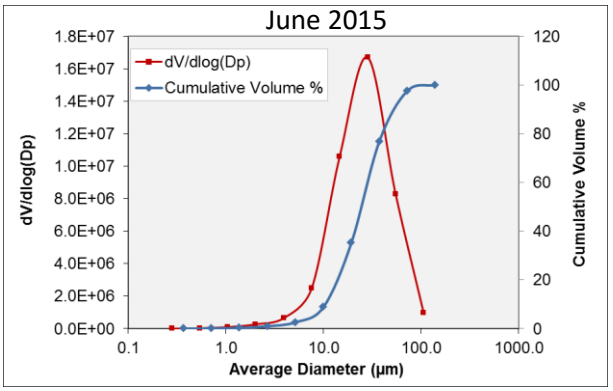

Appendix A

SEM based particle volume distribution curves for 12 months of 2015

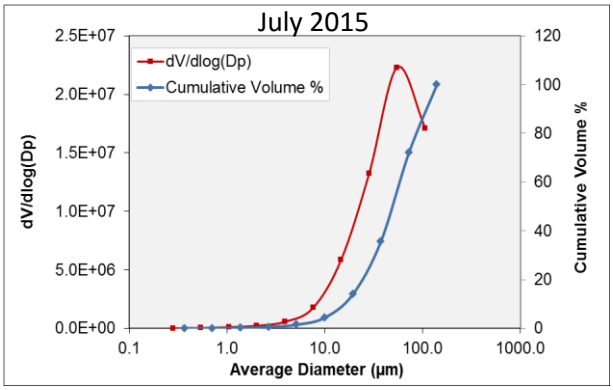

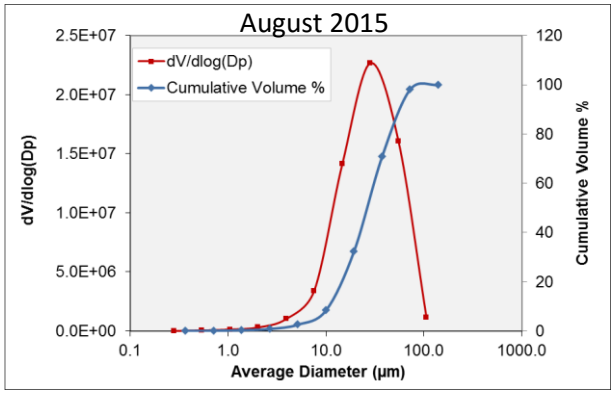

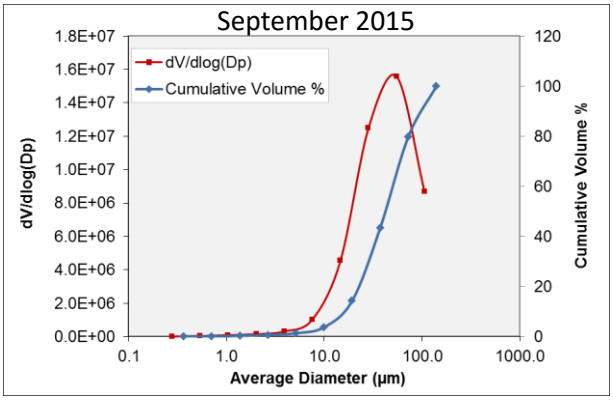

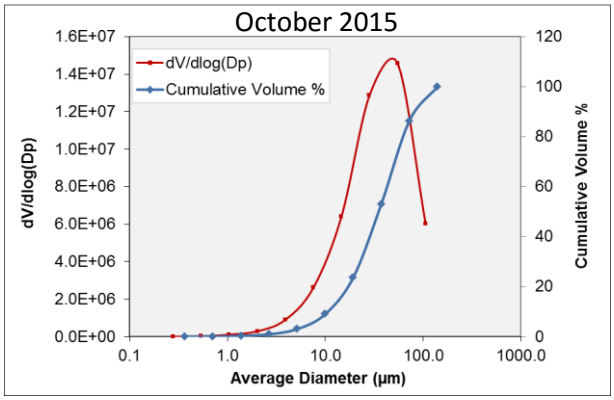

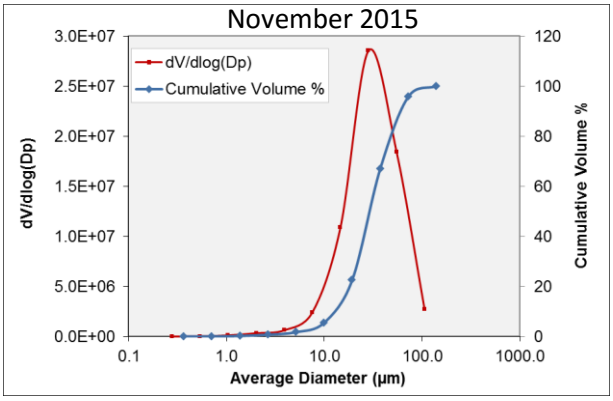

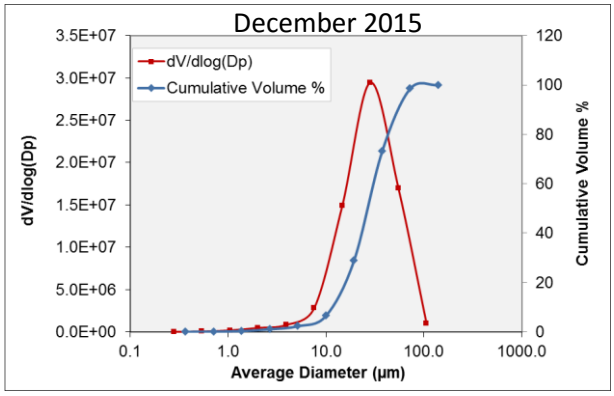

5

Appendix B

Sample	DT1_Jan 2015			DT1_ Feb 2015			DT1_March 2015			DT1_April 2015			DT2_April 2015			DT1_May2015			DT2_ May 2015		
Major and minor elements as oxides (%)																					
SiO_2	27.890	±	0.050	35.886	±	0.065	53.301	±	0.089	38.965	±	0.063	41.802	±	0.073	31.729	±	0.055	21.772	±	0.039
TiO_2	0.466	±	0.001	0.530	±	0.001	0.679	±	0.002	0.464	±	0.002	0.599	±	0.002	0.486	±	0.002	0.451	±	0.001
Al_2O_3	3.505	±	0.035	4.464	±	0.050	5.421	±	0.097	4.257	±	0.115	4.824	±	0.081	3.817	±	0.079	3.033	±	0.026
Fe_2O_3	4.480	±	0.007	5.119	±	0.008	6.312	±	0.013	4.309	±	0.013	5.091	±	0.011	4.150	±	0.010	4.104	±	0.006
MnO	0.080	±	0.001	0.082	±	0.002	0.109	±	0.004	0.075	±	0.005	0.091	±	0.003	0.077	±	0.003	0.066	±	0.001
CaO*	1.989	±	0.015	2.097	±	0.013	4.157	±	0.016	2.369	±	0.018	3.066	±	0.017	0.753	±	0.014	0.847	±	0.013
K_2O*	0.484	±	0.005	0.604	±	0.004	0.864	±	0.003	0.705	±	0.006	0.798	±	0.005	0.542	±	0.008	0.432	±	0.007
P_2O_5	0.417	±	0.001	0.150	±	0.001	0.010	±	0.003	0.332	±	0.004	0.306	±	0.002	0.474	±	0.003	0.429	±	0.001
Total (oxides)	39.311			48.932			70.852			51.475			56.579			42.028			31.134		
Trace elements (ppm)																					
V	107	±	1	76	±	1	85	±	3	106	±	4	93	±	3	116	±	3	99	±	1
Cr	92	±	3	115	±	5	113	±	12	101	±	15	108	±	10	113	±	10	120	±	2
Ni	78	±	2	71	±	3	84	±	6	68	±	8	71	±	5	77	±	5	57	±	1
Cu	81	±	3	57	±	4	134	±	10	125	±	13	99	±	9	206	±	9	64	±	2
Zn	223	±	5	247	±	8	293	±	18	287	±	23	258	±	15	467	±	16	219	±	4
As	0	±	3	0	±	5	6	±	12	0	±	15	0	±	10	0	±	10	0	±	2
Br	29	±	3	26	±	4	42	±	10	59	±	13	45	±	9	34	±	9	76	±	2
Rb	28	±	1	24	±	1	16	±	3	28	±	4	34	±	3	30	±	3	27	±	1
Sr	333	±	3	392	±	5	514	±	11	386	±	13	422	±	9	303	±	9	341	±	2
Y	1071	±	4	36	±	4	26	±	10	125	±	13	46	±	9	36	±	9	24	±	2
Zr	103	±	4	98	±	6	84	±	14	57	±	17	139	±	12	133	±	12	134	±	3
Mo	0	±	5	0	±	7	12	±	17	4	±	21	8	±	14	0	±	14	0	±	3
Pb	15	±	5	28	±	8	32	±	18	66	±	23	28	±	15	19	±	15	28	±	3
Water soluble ions (%)																					
NH_4^+	0.027	±	0.003	0.033	±	0.004	0.055	±	0.006	0.105	±	0.012	0.095	±	0.011	0.076	±	0.009	0.079	±	0.009
Na^+	1.585	±	0.012	1.267	±	0.010	1.053	±	0.009	2.952	±	0.021	2.897	±	0.021	3.519	±	0.025	4.473	±	0.031
K^+	0.230	±	0.009	0.170	±	0.006	0.114	±	0.004	0.262	±	0.010	0.207	±	0.008	0.371	±	0.014	0.296	±	0.011
Mg^{2+}	0.338	±	0.005	0.265	±	0.004	0.188	±	0.003	0.488	±	0.007	0.400	±	0.005	0.558	±	0.008	0.744	±	0.010
Ca^{2+}	3.311	±	0.028	2.718	±	0.023	1.813	±	0.015	3.745	±	0.032	3.220	±	0.027	3.780	±	0.032	3.560	±	0.030
Cl^-	2.563	±	0.014	2.054	±	0.011	1.695	±	0.009	4.177	±	0.022	4.227	±	0.023	3.963	±	0.021	5.927	±	0.032
NO_3^-	0.830	±	0.030	0.843	±	0.031	0.082	±	0.004	0.269	±	0.010	0.051	±	0.004	1.578	±	0.057	0.107	±	0.005
SO_4^{2-}	3.877	±	0.034	2.199	±	0.019	1.718	±	0.015	3.055	±	0.027	2.549	±	0.022	3.527	±	0.031	4.327	±	0.038
Total (ions)	12.761			9.548			6.719			15.052			13.647			17.372			19.513		
Total (oxides + ions)	52.072			58.479			77.571			66.527			70.226			59.400			50.647		
Note: CaO* and K2O* are water insoluble, $P_2O_5^-$ calculated from total P																					

Appendix B

Sample	DT3_May 2015			DT1_June 2015			DT2_June 2015			DT3_June 2015			DT1_ July 2015			DT2_ July 2015			DT3_ July 2015		
Major and minor elements as oxides (%)																					
SiO_2	27.167	±	0.051	28.318	±	0.053	18.530	±	0.035	24.158	±	0.045	13.820	±	0.027	12.693	±	0.025	23.221	±	0.037
TiO_2	0.448	±	0.001	0.478	±	0.002	0.306	±	0.001	0.370	±	0.001	0.261	±	0.001	0.241	±	0.001	0.200	±	0.002
Al_2O_3	3.777	±	0.059	3.692	±	0.062	2.919	±	0.050	3.067	±	0.045	1.886	±	0.041	2.030	±	0.037	2.694	±	0.148
Fe_2O_3	3.972	±	0.008	3.906	±	0.008	2.782	±	0.006	3.346	±	0.006	2.287	±	0.005	2.154	±	0.005	1.935	±	0.014
MnO	0.083	±	0.002	0.077	±	0.002	0.050	±	0.002	0.068	±	0.002	0.050	±	0.002	0.044	±	0.002	0.050	±	0.007
CaO*	1.983	±	0.016	1.681	±	0.014	1.179	±	0.013	1.745	±	0.014	0.427	±	0.010	1.179	±	0.011	1.148	±	0.013
K_2O*	0.508	±	0.006	0.513	±	0.007	0.366	±	0.008	0.467	±	0.006	0.208	±	0.008	0.226	±	0.008	0.359	±	0.009
P_2O_5	0.170	±	0.002	0.590	±	0.002	0.383	±	0.002	0.389	±	0.001	0.753	±	0.002	0.457	±	0.001	0.288	±	0.005
Total (oxides)	38.108			39.254			26.514			33.609			19.692			19.024			29.895		
Trace elements (ppm)																					
V	88	±	2	111	±	2	86	±	2	91	±	1	115	±	1	111	±	1	77	±	5
Cr	71	±	7	96	±	7	65	±	6	82	±	5	160	±	5	60	±	5	67	±	21
Ni	62	±	3	84	±	4	49	±	3	72	±	3	133	±	3	71	±	2	91	±	11
Cu	56	±	6	134	±	7	59	±	5	49	±	5	209	±	5	62	±	4	25	±	19
Zn	251	±	11	430	±	12	297	±	9	255	±	8	515	±	9	244	±	7	180	±	32
As	0	±	7	0	±	7	0	±	6	0	±	5	0	±	5	0	±	5	0	±	21
Br	58	±	6	62	±	7	100	±	5	64	±	5	62	±	5	88	±	4	37	±	19
Rb	24	±	2	35	±	2	16	±	2	23	±	1	17	±	1	12	±	1	8	±	5
Sr	392	±	7	322	±	7	276	±	6	291	±	5	233	±	5	268	±	4	284	±	19
Y	14	±	6	23	±	7	14	±	5	19	±	5	7	±	5	12	±	4	23	±	19
Zr	123	±	8	149	±	9	112	±	7	82	±	6	76	±	6	83	±	6	88	±	24
Mo	0	±	10	0	±	10	0	±	8	0	±	7	0	±	7	0	±	6	0	±	29
Pb	18	±	10	12	±	11	15	±	9	17	±	8	22	±	8	30	±	7	45	±	32
Water soluble ions (%)																					
NH_4^+	0.091	±	0.010	0.125	±	0.014	0.120	±	0.013	0.100	±	0.011	0.088	±	0.010	0.032	±	0.004	0.109	±	0.012
Na^+	4.509	±	0.031	3.505	±	0.025	5.875	±	0.041	2.834	±	0.020	3.466	±	0.024	5.538	±	0.038	5.360	±	0.037
K^+	0.276	±	0.010	0.312	±	0.012	0.352	±	0.013	0.256	±	0.010	0.339	±	0.013	0.360	±	0.013	0.390	±	0.015
Mg^{2+}	0.572	±	0.008	0.559	±	0.008	0.947	±	0.013	0.453	±	0.006	0.582	±	0.008	0.878	±	0.012	0.628	±	0.009
Ca^{2+}	3.582	±	0.030	3.094	±	0.026	3.341	±	0.028	3.092	±	0.026	2.767	±	0.024	2.642	±	0.022	2.833	±	0.024
Cl^-	6.828	±	0.037	3.648	±	0.020	7.799	±	0.042	3.562	±	0.019	3.141	±	0.017	6.005	±	0.032	7.612	±	0.041
NO_3^-	1.328	±	0.048	0.595	±	0.022	0.349	±	0.013	0.939	±	0.034	1.573	±	0.057	1.702	±	0.061	1.864	±	0.067
SO_4^{2-}	3.649	±	0.032	2.965	±	0.026	4.878	±	0.043	2.483	±	0.022	2.923	±	0.026	4.424	±	0.039	3.087	±	0.027
Total (ions)	20.836			14.804			23.663			13.719			14.879			21.580			21.882		
Total (oxides + ions)	58.944			54.058			50.177			47.328			34.571			40.605			51.777		
Note: CaO* and K2O* are water insoluble, $P_2O_5^-$ calculated from total P																					

Appendix B

Sample	DT1_Aug 2015			DT2_Aug 2015			DT3_Aug 2015			DT1_Sept_2015			DT2_Sept_2015			DT3_Sept_2015			DT1_Oct 2015		
Major and minor elements as oxides (%)																					
SiO_2	34.862	±	0.061	33.619	±	0.058	29.244	±	0.054	50.971	±	0.083	11.690	±	0.024	42.544	±	0.074	41.270	±	0.067
TiO_2	0.591	±	0.001	0.469	±	0.002	0.422	±	0.002	0.605	±	0.003	0.206	±	0.001	0.609	±	0.002	0.496	±	0.002
Al_2O_3	4.021	±	0.033	3.773	±	0.078	3.514	±	0.068	5.057	±	0.124	3.628	±	0.053	5.114	±	0.081	4.374	±	0.115
Fe_2O_3	5.488	±	0.008	4.186	±	0.010	3.878	±	0.009	5.479	±	0.015	2.206	±	0.006	5.540	±	0.011	4.592	±	0.013
MnO	0.095	±	0.001	0.082	±	0.003	0.068	±	0.003	0.102	±	0.005	0.048	±	0.002	0.096	±	0.003	0.081	±	0.005
CaO*	1.772	±	0.014	5.067	±	0.017	3.423	±	0.014	4.909	±	0.019	3.273	±	0.006	0.598	±	0.014	2.690	±	0.018
K_2O*	0.598	±	0.003	0.850	±	0.002	0.709	±	0.003	0.988	±	0.002	0.000	±	0.014	0.853	±	0.003	0.756	±	0.004
P_2O_5	0.249	±	0.001	0.158	±	0.002	0.076	±	0.002	0.000	±	0.004	0.000	±	0.001	0.194	±	0.002	0.047	±	0.003
Total (oxides)	47.676			48.204			41.334			68.110			21.051			55.547			54.306		
Trace elements (ppm)																					
V	122	±	1	110	±	3	42	±	2	51	±	4	19	±	2	93	±	2	0	±	4
Cr	116	±	3	59	±	10	76	±	9	96	±	16	46	±	6	93	±	10	152	±	15
Ni	91	±	1	71	±	5	54	±	4	61	±	8	29	±	3	76	±	5	73	±	8
Cu	55	±	2	76	±	9	41	±	7	55	±	14	32	±	5	86	±	8	40	±	13
Zn	194	±	4	226	±	15	127	±	13	157	±	24	107	±	9	339	±	15	185	±	23
As	0	±	3	0	±	10	0	±	9	0	±	16	0	±	6	0	±	10	0	±	15
Br	20	±	2	16	±	9	34	±	7	17	±	14	715	±	7	58	±	8	64	±	13
Rb	22	±	1	43	±	3	12	±	2	47	±	4	18	±	2	38	±	2	24	±	4
Sr	441	±	3	369	±	9	257	±	7	394	±	14	179	±	5	345	±	9	331	±	13
Y	18	±	2	9	±	9	25	±	7	23	±	14	8	±	5	14	±	8	18	±	13
Zr	141	±	3	133	±	12	125	±	10	123	±	20	62	±	7	127	±	12	99	±	17
Mo	0	±	4	0	±	14	0	±	12	0	±	23	1	±	8	3	±	13	17	±	21
Pb	4	±	4	58	±	15	63	±	13	36	±	24	12	±	9	28	±	14	46	±	23
Water soluble ions (%)																					
NH_4^+	0.025	±	0.003	0.018	±	0.002	0.021	±	0.002	0.021	±	0.003	0.027	±	0.003	0.024	±	0.003	0.013	±	0.002
Na^+	1.044	±	0.009	0.481	±	0.006	1.144	±	0.009	0.756	±	0.007	12.685	±	0.087	0.862	±	0.008	2.134	±	0.016
K^+	0.116	±	0.004	0.094	±	0.004	0.133	±	0.005	0.106	±	0.004	0.625	±	0.023	0.123	±	0.005	0.192	±	0.007
Mg^{2+}	0.213	±	0.003	0.133	±	0.002	0.193	±	0.003	0.146	±	0.002	1.732	±	0.024	0.261	±	0.004	0.425	±	0.006
Ca^{2+}	3.101	±	0.026	1.772	±	0.015	1.840	±	0.016	2.143	±	0.018	1.280	±	0.011	1.928	±	0.016	3.415	±	0.029
Cl^-	1.624	±	0.009	0.588	±	0.004	1.460	±	0.008	1.216	±	0.007	23.054	±	0.123	1.034	±	0.006	3.267	±	0.018
NO_3^-	1.045	±	0.038	0.418	±	0.015	0.943	±	0.034	0.396	±	0.015	0.007	±	0.003	0.004	±	0.003	0.009	±	0.003
SO_4^{2-}	3.241	±	0.028	1.425	±	0.012	1.591	±	0.014	2.047	±	0.018	2.778	±	0.024	1.743	±	0.015	3.042	±	0.027
Total (ions)	10.410			4.930			7.324			6.831			42.187			5.980			12.496		
Total (oxides + ions)	58.085			53.134			48.658			74.941			63.238			61.527			66.802		
Note: CaO* and K2O* are water insoluble, $P_2O_5^-$ calculated from total P																					

Appendix B

Sample	DT2_Oct 2015			DT3_Oct 2015			DT1_Nov 2015			DT2_Nov 2015			DT3_Nov 2015			DT1_Dec 2015			DT2_Dec 2015			DT3_Dec 2015		
Major and minor elements as oxides (%)																								
SiO_2	14.274	±	0.028	38.421	±	0.068	42.440	±	0.076	23.596	±	0.044	38.454	±	0.070	33.248	±	0.059	28.716	±	0.053	28.860	±	0.052
TiO_2	0.206	±	0.001	0.587	±	0.001	0.687	±	0.002	0.481	±	0.001	0.651	±	0.002	0.653	±	0.001	0.486	±	0.001	0.507	±	0.001
Al_2O_3	3.483	±	0.048	4.611	±	0.045	5.114	±	0.052	3.202	±	0.046	5.353	±	0.069	4.657	±	0.040	3.472	±	0.055	3.603	±	0.038
Fe_2O_3	2.118	±	0.005	5.577	±	0.008	6.509	±	0.010	4.736	±	0.008	7.170	±	0.012	6.180	±	0.009	4.276	±	0.008	4.597	±	0.007
MnO	0.041	±	0.002	0.103	±	0.001	0.125	±	0.002	0.119	±	0.002	0.121	±	0.003	0.121	±	0.001	0.085	±	0.002	0.079	±	0.001
CaO*	5.742	±	0.008	3.357	±	0.015	0.731	±	0.021	1.586	±	0.010	2.370	±	0.008	2.321	±	0.011	1.965	±	0.015	2.502	±	0.014
K_2O*	0.090	±	0.010	0.774	±	0.002	0.822	±	0.002	0.552	±	0.003	0.954	±	0.002	0.751	±	0.002	0.590	±	0.003	0.592	±	0.003
P_2O_5	0.000	±	0.001	0.106	±	0.001	0.000	±	0.001	0.145	±	0.001	0.181	±	0.002	0.133	±	0.001	0.155	±	0.002	0.102	±	0.001
Total (oxides)	25.953			53.537			56.429			34.418			55.254			48.064			39.745			40.840		
Trace elements (ppm)																								
V	67	±	1	125	±	1	130	±	1	149	±	2	180	±	2	144	±	1	97	±	2	65	±	1
Cr	26	±	5	110	±	4	119	±	5	300	±	6	135	±	8	218	±	4	103	±	7	71	±	4
Ni	33	±	3	84	±	2	68	±	2	971	±	3	121	±	4	211	±	2	134	±	3	64	±	2
Cu	28	±	5	111	±	4	59	±	4	102	±	5	74	±	7	78	±	3	89	±	6	55	±	3
Zn	82	±	8	250	±	7	205	±	8	507	±	9	358	±	12	534	±	6	328	±	10	231	±	6
As	0	±	5	0	±	4	0	±	5	0	±	5	0	±	8	0	±	3	0	±	7	3	±	4
Br	457	±	5	27	±	4	56	±	4	66	±	5	61	±	7	59	±	3	112	±	6	95	±	4
Rb	11	±	1	40	±	1	35	±	1	26	±	1	34	±	2	27	±	1	22	±	2	22	±	1
Sr	227	±	5	422	±	4	683	±	5	253	±	5	210	±	7	329	±	3	266	±	6	310	±	4
Y	14	±	5	13	±	4	14	±	4	15	±	5	39	±	7	23	±	3	13	±	6	19	±	3
Zr	38	±	6	134	±	5	143	±	6	103	±	6	192	±	10	139	±	4	113	±	8	95	±	5
Mo	0	±	7	1	±	6	0	±	7	3	±	7	0	±	10	1	±	5	3	±	9	0	±	5
Pb	8	±	8	36	±	6	17	±	7	20	±	8	24	±	11	22	±	5	30	±	10	40	±	6
Water soluble ions (%)																								
NH_4^+	0.047	±	0.005	0.043	±	0.005	0.028	±	0.003	0.024	±	0.003	0.025	±	0.003	0.032	±	0.004	0.011	±	0.001	0.025	±	0.003
Na^+	10.668	±	0.073	0.577	±	0.006	0.675	±	0.007	0.890	±	0.008	0.684	±	0.007	0.699	±	0.007	1.279	±	0.010	1.540	±	0.012
K^+	0.447	±	0.017	0.086	±	0.003	0.106	±	0.004	0.125	±	0.005	0.072	±	0.003	0.081	±	0.003	0.136	±	0.005	0.135	±	0.005
Mg^{2+}	1.315	±	0.018	0.164	±	0.002	0.143	±	0.002	0.185	±	0.003	0.066	±	0.001	0.095	±	0.001	0.232	±	0.003	0.225	±	0.003
Ca^{2+}	2.543	±	0.022	2.506	±	0.021	1.851	±	0.016	2.059	±	0.018	0.573	±	0.005	1.949	±	0.017	3.422	±	0.029	2.815	±	0.024
Cl^-	18.796	±	0.101	0.910	±	0.005	1.181	±	0.006	1.246	±	0.007	1.071	±	0.006	1.120	±	0.006	2.083	±	0.011	2.494	±	0.013
NO_3^-	0.009	±	0.003	0.007	±	0.003	0.029	±	0.003	0.004	±	0.003	0.007	±	0.003	0.033	±	0.003	0.205	±	0.008	0.026	±	0.003
SO_4^{2-}	3.581	±	0.031	1.411	±	0.012	1.133	±	0.010	2.297	±	0.020	0.697	±	0.006	1.734	±	0.015	2.188	±	0.019	1.964	±	0.017
Total (ions)	37.407			5.704			5.146			6.831			3.196			5.745			9.558			9.224		
Total (oxides + ions)	63.360			59.240			61.574			41.249			58.450			53.810			49.303			50.065		
Note: CaO* and K2O* are water insoluble, $P_2O_5^-$ calculated from total P																								

Supplement A

Sampling Sites Meta-data

The NEO sampling site (DT3, DT4) is within a fenced area about 200 m in length and 50 m in width, situated along the southeastern border of the KAUST campus. The soil surface is covered by a layer of gravel and paved walkways, to contain local dust emissions. The Frisbee deposition samplers as well as several experimental photovoltaic (PV) and meteorological systems are installed at the NEO site. Besides the regional dust, the site is impacted by local emissions from vehicles traveling along the paved road to the south and in the paved parking lot to the north. Depending on the wind, the site was periodically exposed to dirt road and construction dust from building activities immediately outside the KAUST campus.

The CMOR sampling site (DT3) is on a concrete paved quay about 200 m in length and 50 m wide, providing docking facilities for small and medium size boats in the KAUST harbor. The deposition sampler was set up close to the furthest edge of the quay, approximately 5m from the water's edge, about 1m above the water line, and approximately 65 m from the CMOR building entrance. The sampler is exposed to local emissions from cargo loading activities and other traffic, as well as sea spray during stormy conditions.

One Frisbee sampler (DT1) was installed on the pebble covered flat garage rooftop of a residential home (G3705), located approximately 1.5 km to the beach area in the west and about 1 km from the harbor to the south. The site is impacted by local paved road traffic, a nearby bus terminal, and activities at a local shopping center. The sampler was set about 5m above the street level, and to some extent above street level dust and local transport emissions.

Supplement B

Dust Deposition on Solar Panels

Dust deposits on solar panels are known to have a severe detrimental effect on the efficiency of photovoltaic systems (Goossens and Van Kerschaever, 1999; Hamou et al., 2014; Mejia et al., 2014; Rao et al., 2014; Sulaiman et al., 2014; Ilse et al., 2016). High humidity is experienced at KAUST throughout the year, more often during the late summer months of July to September. This is reflected by dew being formed on radiating cool surfaces such as solar panels, as well as coastal fog during the early morning hours. The gypsum component of dust being collected by the Frisbee samplers and on all exposed surfaces is being partly dissolved by the dew, and on drying being recrystallized. XRD measurements performed directly on dust collected on zero background silicon wafers exposed over a period of several months showed the dust surface to be hardened by the crystallization of blades of gypsum. These surface crusts of gypsum were shown to have a distinct preferred orientation, having their (010) crystal planes parallel to the surface of the silicon wafer, as will be the case on other flat surfaces. The cementation of dust on glass surfaces by gypsum encrustation increases the adhesion of dust on the solar panels, and a resultant attenuation of solar panel efficiency. Dust mineralogy and mineralogical interrelationships, together with climatic conditions are variables determining the nature of dust deposits on solar panels. This needs to be understood with the planning and placement of solar arrays.

Supplement C

SEM based particle number distribution curves for 12 months of 2015

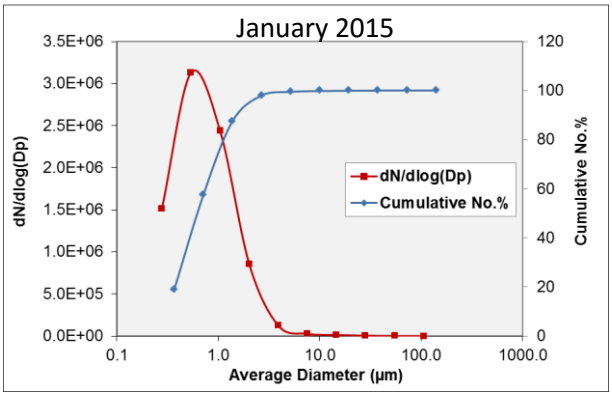

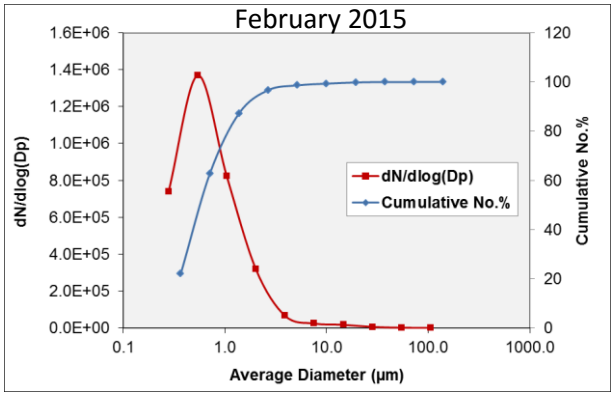

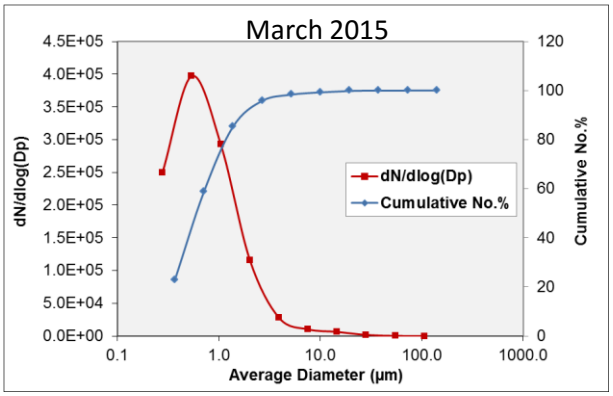

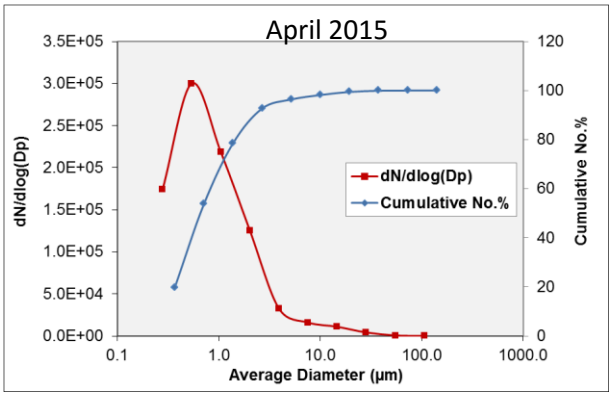

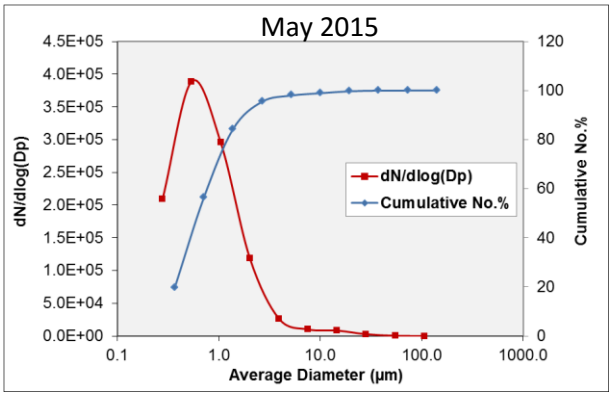

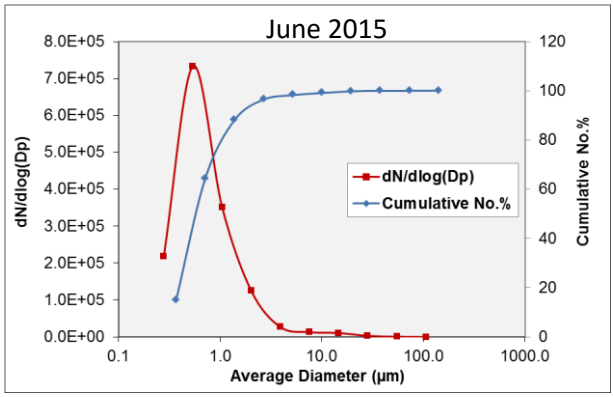

5

Supplement C

SEM based particle number distribution curves for 12 months of 2015

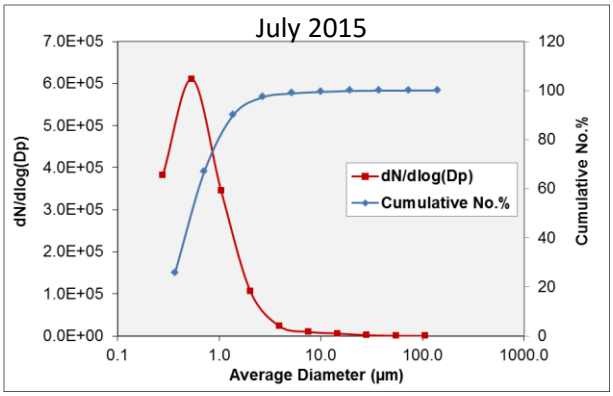

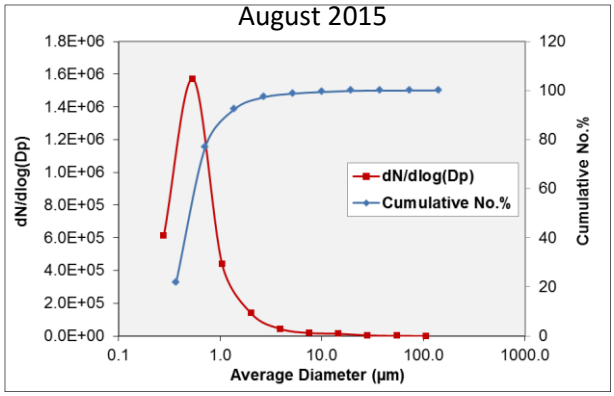

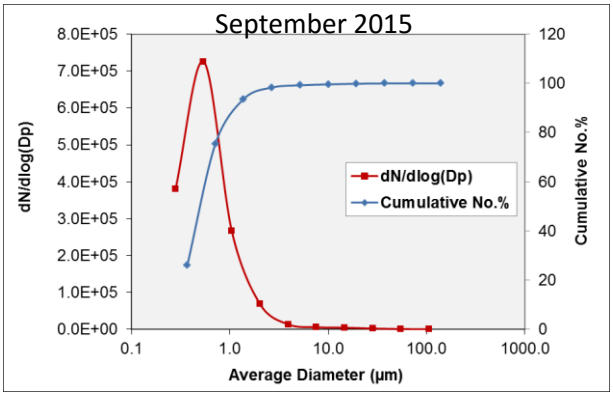

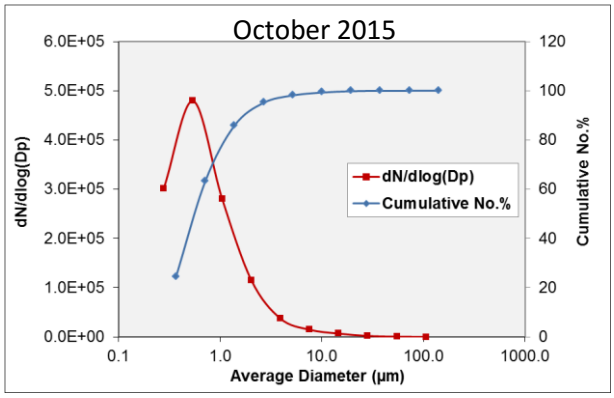

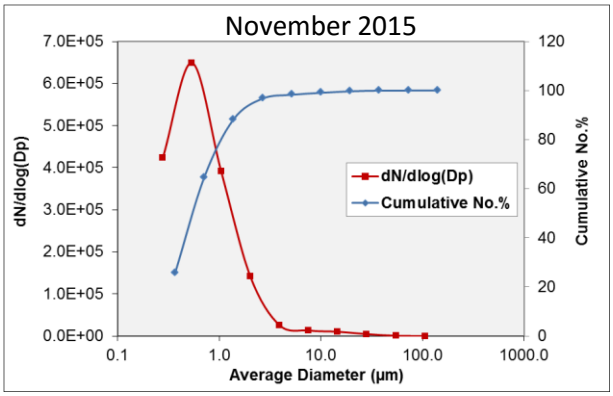

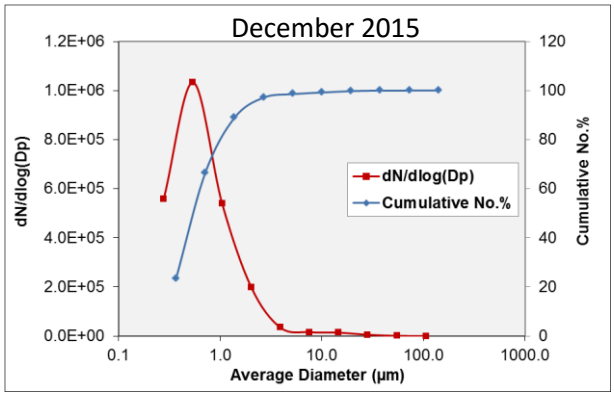

5